On the formulation and implementation of extrinsic cohesive zone models with contact

Nicholas Anton Collins-Craft, Franck Bourrier, Vincent Acary

On the formulation and implementation of extrinsic cohesive zone models with contact

N. A. Collins-Craft, F. Bourrier, V. Acary

October 8, 2021

Contents

Notation For vector and tensors, we choose the following notation:

$$\|\boldsymbol{x}\|^2 = \|x\|^2 = \underbrace{x_i x^i}_{\text{indicial notation}} = \underbrace{\boldsymbol{x}.\boldsymbol{x}}_{\text{tensor notation}} = \underbrace{x^\top x}_{\text{vector notation}} \tag{1}$$

1 Introduction

The modelling of crack propagation touches on a wide variety of areas of interest within mechanics, ranging from a geological scale (Okubo et al., 2019) to the very fine details of composite materials (Ashouri Vajari et al., 2013). While linear elastic fracture mechanics (LEFM), pioneered by Griffith (1921), accurately describes significant aspects of crack behaviour, it suffers from the presence of a stress singularity at the crack tip, rendering the model non-physical in the "fracture process zone", the region surrounding the crack tip. In order to model situations where individual cracks have a large effect on the overall structural behaviour of a system such as fragmentation or dynamic crack branching problems, researchers make use of cohesive zone models (see seminal articles such as Nguyen and Wu (2018), Xu and Needleman (1994), and Zhang et al. (2007)). Cohesive zone models regularise the LEFM stress singularity at the crack tip by expressing a relationship between the displacement jump across a developing crack surface and the traction that the surface can support. The total area under the traction-displacement curve represents the classical fracture energy of LEFM (Griffith, 1921). In cohesive zone models the evolution of this interface is described in terms of a cohesion variable $\beta \in [0, 1]$, where $\beta = 1$ indicates a perfectly intact interface, and $\beta = 0$ a completely broken interface.

Direct experimental observation of the fracture process zone is extremely difficult, due to their typically small size (depending on the material, as small as the order of 10nm (Azab et al., 2020)) and rapid motion. Very few direct observations have been made (Célarié

et al., 2003; Guilloteau et al., 1996), although recent work studying the cohesive zones of frictional cracks (Berman et al., 2020) offers a promising path towards further direct observations. Due to this difficulty of direct observation, the properties of the cohesive zone are typically inferred via experimental observations at a larger scale. It should be noted that the particular values of the inferred parameters such as total fracture energy G_c, critical traction σ_c and critical length δ_c depend on the exact form of the cohesive zone model chosen (Azab et al., 2020). Some inference as to the appropriate form of the model may be drawn by comparing back-analyses of experiments via cohesive zone models with those conducted using other crack analysis techniques such as the coupled criterion (Doitrand et al., 2019).

While the particular form of cohesive zone models is arbitrary and limited only by the modeller's imagination, in a broad sense they may all be categorised as one of two flavours, intrinsic and extrinsic models. Intrinsic models include an initially elastic response, with an initial strengthening of the cohesive zone as a function of the displacement jump, before weakening due to the decohesion process (Falk et al., 2001). As a consequence, there is an additional length parameter, the hardening length δ_h, where the cohesive traction obtains its maximum value (Kubair and Geubelle, 2003). Intrinsic cohesive elements are inserted between the mesh elements before simulation, leading to straightforward computational parallelisation (Nguyen, 2014). However, the elasticity present in the intrinsic model has the effect of modifying the overall elasticity of the structure, with this effect becoming more significant with a greater number of cohesive elements. Thus, intrinsic models introduce an unwanted mesh-dependency to the problem (Falk et al., 2001). The problem of induced artificial compliance can be reduced by increasing the initial hardening slope of the cohesive law. However, in dynamic analyses, this stiffness increase results in severe restrictions on the stable time-step size, rendering the method essentially unsuitable (Nguyen, 2014). The presence of interface elasticity also allows for the possibility of interpenetration and physically meaningless negative displacement jumps if the two sides of the interface are pushed together (Acary and Monerie, 2006). Finally, we also note the conceptual impossibility of measuring interface stiffness across a crack face before the crack exists, meaning that any stiffness assigned in an intrinsic model must necessarily be arbitrary and not representative of a true physical property.

On the other hand, extrinsic models are initially rigid and hence immediately start to decohere as the displacement jump increases (Kubair and Geubelle, 2003; Seagraves and Radovitzky, 2010). These models do not effect the elasticity of the bulk, however, typically they are inserted adaptively on-the-fly into finite element meshes (Zhou and Molinari, 2004a), as pre-inserting the elements leads to very large computational overheads due to each node requiring duplicates. Historically the on-the-fly insertion has meant that extrinsic models were difficult to parallelise (Carter et al., 2000), but modern techniques have been developed that have overcome the previous difficulties (Espinha et al., 2013). The absence of artificial stiffness in the extrinsic formulation renders it suitable for use in dynamic analyses due to the absence of artificial compliance effects (Camacho and Ortiz, 1996; Murphy and Ivankovic, 2005; Seagraves and Radovitzky, 2010), but care must be taken to ensure that the system exhibits time-continuous behaviour (Papoulia et al., 2003; Sam et al., 2005). While extrinsic models do not have the pathological mesh-dependency of intrinsic models, the large number of elements required to fully resolve the cohesive zone for arbitrary crack paths has been impractical, meaning that simulations are typically not fully converged. This issue can be at least partially addressed by modelling cohesive zone strength via a Weibull distribution (Zhou and Molinari, 2004a; Zhou and Molinari, 2004b). The use of more sophisticated finite element techniques such as those based on the partition of unity (Bybordiani and Dias-da-Costa, 2021), Hybrid Equilibrium Elements (Parrinello, 2020; Parrinello and Borino, 2020), or Discontinuous Galerkin (Nguyen, 2014; Versino et al., 2015) constitutes a promising path towards truly mesh-independent results.

However, we must also pay close attention to the unload-reload behaviour of models, particularly in cases of non-monotonic loading e.g. repeated impacts or complex stress wave patterns, where cohesive elements may incur only partial decohesion before being subjected to unloading and reloading. By considering the mathematical structure detailed in Kubair and Geubelle (2003), where by shifting the values of model parameters both intrinsic and extrinsic models may be obtained from the same formula, we may define the notion of a "shifted intrinsic model", where the extrinsic model retains an underlying intrinsic mathematical structure. Typically extrinsic models indicate that after the cohesion has decreased, the unload-reload behaviour is elastic until decohesion recommences (Bybordiani and Dias-da-Costa, 2021; Camacho and Ortiz, 1996; Parrinello, 2020; Parrinello and Borino, 2020; Sam et al., 2005). Models exhibiting this behaviour constitute shifted intrinsic models where the *effective* critical traction $\sigma_{c,e}$ and hardening length δ_h are shifted away from their initial values (σ_c and 0 respectively) as the cohesion β evolves. For this family of models, the unload-reload elasticity can be approximated by $E \approx \tan\left(\beta\frac{\pi}{2}\right)$. It is clear that for very small amounts of decohesion with $\beta \approx 1$, the elasticity of the interface is arbitrarily large and the problems of artificial compliance inherent to intrinsic models may also arise in extrinsic models if they have the shifted intrinsic model structure.

Thus, we may conclude that an extrinsic model is the most appropriate to model crack behaviour, but special care must be taken to avoid unphysical behaviour at the interface in both the initial loading phase, and for cases of unloading and reloading. To this end, we turn to the field of contact mechanics, in particular the seminal work of Moreau (Moreau, 1970, 1974, 1986), who developed the mathematical framework of non-smooth mechanics. By appropriately specifying the potential of energy and the pseudo-potential of dissipation within the framework of Convex Analysis, rigorous thermodynamic formulations for a range of materials may be developed (Houlsby, 2019; Marigo, 1981). In particular, this family of models has been extended to cohesive zone modelling in a series of seminal works by Frémond (Frémond, 1988, 2002, 2012a,b), which provides a natural framework in which we present our models.

Novelty of the contribution and outline of the article: The novelty of our work is that we present the formulation of an extrinsic model that cleanly separates the effects of dynamic contact with those of the cohesive zone, exploiting the framework of non-smooth

mechanics. The model does not have the shifted intrinsic model structure, and so avoids the associated problematic unload-reload behaviour. Importantly, we are able to write the model in terms of a linear complementarity problem (LCP) that may be solved monolithically, allowing us to exploit the efficient algorithms that have been developed for this class of problems. Finally, we apply the model to some pertinent example systems and compare the results with those obtained by other workers.

2 Formulation of extrinsic cohesive models with contact

2.1 State variables, powers and principle of virtual power

Let us consider a body defined by $\Omega \in \mathbb{R}^d, d \in [\![1,3]\!]$. The vector x defines the current position and X the initial position, $u(x)$ the displacement and $v(x) = \dot{u}(x)$ the velocity. The definition of the displacement jump is the interface is not trivial in practice. In this work, we consider that, initially, the material is undamaged. At a point $x \in \Omega, x \in \mathbb{R}^d$, the displacement $u(x)$ and the velocity $v(x)$ are continuously differentiable functions of x. If a crack occurs and an interface is created, two material points x_l and x_r are defined by splitting the bodies assuming that they correspond to the material point X initially. We choose to denote x_l by x. The displacement jump is defined by the difference in the position of the material point that was at X initially, with respect to x and x_r, that is $[\![u(x, x_r)]\!] = u(x_r) - u(x)$. We also assume that we are able to define an orthonormal local frame at any point x of the interface defined by (x, N, T) where $N \in \mathbb{R}^d$ is the normal unit vector from x towards x_r and the vector $[T_1, T_2] \in \mathbb{R}^{d\times d-1}$ completes the frame. In this work, we consider only the normal displacement (jump), defined by $u_{\text{N}}(x, x_r) = [\![u(x, x_l)]\!]N \in \mathbb{R}$. The relative velocity (jump in space) is defined as $v_{\text{N}} = \dot{u}_{\text{N}}$. Before the creation of the interface, we assume that u_{N} and v_{N} vanish whatever the arbitrary definition of the local frame since u and v are continuous.

To describe the state of the cohesion we introduce the cohesion variable $\beta(x) \in [0, 1]$, using the notation introduced by Frémond for describing the intensity of cohesion, or the proportion of active bonds. For a point x on the interface, the power of the cohesion for a surface Γ is defined by

$$\mathcal{P}_{\mathsf{coh}} = \int_\Gamma \dot{\beta} A \,\mathrm{d}x \tag{2}$$

introducing A which is the dual force (driving force) associated to β. In the same way, the power of contact is given by

$$\mathcal{P}_{\mathsf{con}} = \int_\Gamma v_{\text{N}}^\top r_{\text{N}} \,\mathrm{d}x \tag{3}$$

introducing r_{N} as the normal reaction force related to the stress $\boldsymbol{\sigma}(x)$ at the interface by $r_{\text{N}} = -\boldsymbol{\sigma} \cdot N$.

For the material in Ω, the power of the external, internal and inertial forces are respectively given by

$$\mathcal{P}_{\mathsf{ext}} = \int_\Omega v^\top f \,\mathrm{d}x - \int_{\Gamma_{\mathcal{N}}} v^\top T \,\mathrm{d}x - \int_\Gamma \dot{\beta} F \,\mathrm{d}x, \tag{4}$$

$$\mathcal{P}_{\mathsf{int}} = -\int_\Omega \boldsymbol{\sigma} : \dot{\boldsymbol{\varepsilon}} \,\mathrm{d}x + \int_\Gamma v_{\text{N}}^\top r_{\text{N}} \,\mathrm{d}x + \int_\Gamma \dot{\beta} A \,\mathrm{d}x, \tag{5}$$

$$\mathcal{P}_{\mathsf{acc}} = \int_\Omega \rho v^\top \dot{v} \,\mathrm{d}x. \tag{6}$$

where f is the body force in Ω, T is the surface traction on $\Gamma_{\mathcal{N}}$ (i.e. where the Neumann boundary condition is applied on the surface), F is an external force that does work on the cohesion (such as may arise from thermal or chemical effects) that is taken as identically zero in this work, $\boldsymbol{\varepsilon}$ is the strain in Ω, ρ is the density and $\dot{v}$ is the acceleration.

The principle of virtual power states that for any virtual velocities $\bar{v}$, $\dot{\bar{\boldsymbol{\varepsilon}}}$ and $\dot{\bar{\beta}}$, we have

$$\begin{aligned} \bar{\mathcal{P}}_{\mathsf{acc}} &= \bar{\mathcal{P}}_{\mathsf{ext}} + \bar{\mathcal{P}}_{\mathsf{int}}, \\ \int_\Omega \rho \bar{v}^\top \dot{v} \,\mathrm{d}x &= \int_\Omega \bar{v}^\top f \,\mathrm{d}x - \int_{\Gamma_{\mathcal{N}}} \bar{v}^\top T \,\mathrm{d}x - \int_\Gamma \dot{\bar{\beta}} F \,\mathrm{d}x - \int_\Omega \boldsymbol{\sigma} : \dot{\bar{\boldsymbol{\varepsilon}}} \,\mathrm{d}x + \int_\Gamma \bar{v}_{\text{N}}^\top r_{\text{N}} \,\mathrm{d}x + \int_\Gamma \dot{\bar{\beta}} A \,\mathrm{d}x \end{aligned} \tag{7}$$

For a rigorous mathematical setting of this principle, we refer to Frémond (1988). Using sufficient smoothness assumptions on the fields, this leads by localization to the set of equations describing the equilibrium and boundary conditions of the system:

$$\begin{cases} \nabla \cdot \boldsymbol{\sigma} + f = \rho \dot{v}, & \text{in } \Omega \\ A = F = 0, & \text{on } \Gamma \\ T = \boldsymbol{\sigma} \cdot N, & \text{on } \Gamma_{\mathcal{N}} \\ r_{\text{N}} = -\boldsymbol{\sigma} \cdot N & \text{on } \Gamma. \end{cases} \tag{8}$$

2.2 A non-smooth thermo-mechanics potential in the normal direction

Free energy and reversible state laws. The free energy of the system is the sum of the free energy in the bulk with that of the surface, that is

$$\int_\Omega \Psi_e(\varepsilon)\,\mathrm{d}x + \int_\Gamma \Psi_s(u_{\mathrm{N}},\beta)\,\mathrm{d}x \tag{9}$$

where Ψ_e and Ψ_s are the volume and surface free energies. In this work, we assume all strain is elastic. Firstly, the stresses may be obtained by assuming a classical linear elastic potential for the bulk:

$$\Psi_e(\varepsilon) = \frac{1}{2}\varepsilon : E : \varepsilon, \tag{10}$$

$$\sigma(\varepsilon) = \frac{\partial \Psi_e(\varepsilon)}{\partial \varepsilon} = E : \varepsilon, \tag{11}$$

where E is a fourth order stiffness tensor. The stress-like variables are similarly derived from the surface potential by

$$\begin{cases} -r_{\mathrm{N}}^{\mathsf{r}} \in \partial_{u_{\mathrm{N}}} \Psi_s(u_{\mathrm{N}},\beta), \\ -A^{\mathsf{r}} \in \partial_{\beta} \Psi_s(u_{\mathrm{N}},\beta), \end{cases} \tag{12}$$

where r_{N}^{r} stands for the reversible part of the normal reaction force, and ∂u_{N} and ∂_β indicate the subdifferentials with respect to u_{N} and β of a convex but non-smooth potential. The first assumption in our model is that the displacement is constrained to be positive, $u_{\mathrm{N}} \geqslant 0$, which is enforced as a unilateral constraint, and the cohesion variable constraints are $0 \leqslant \beta \leqslant 1$. This yields the possible form of the surface free energy

$$\Psi_s(u_{\mathrm{N}},\beta) = \psi(u_{\mathrm{N}},\beta) + \mathcal{I}_{\mathbb{R}_+}(u_{\mathrm{N}}) + \mathcal{I}_{[0,1]}(\beta), \tag{13}$$

where $\mathcal{I}_C$ is the indicator function of a convex set C. To obtain an extrinsic CZM, the tangent stiffness of the model when $u_{\mathrm{N}} \geqslant 0$ must vanish. In other words, the derivative of $\psi(u_{\mathrm{N}},\beta)$ with respect to u_{N} must be constant, *i.e.* $\dfrac{\partial^2 \psi}{\partial {u_{\mathrm{N}}}^2} = 0$. The simplest choice for the free energy is:

$$\Psi_s(u_{\mathrm{N}},\beta) = \beta\sigma_c u_{\mathrm{N}} + w f(\beta) + \mathcal{I}_{\mathbb{R}_+}(u_{\mathrm{N}}) + \mathcal{I}_{[0,1]}(\beta), \tag{14}$$

where

- $\sigma_c > 0$ is the critical traction,
- $w > 0$ is the surface free energy which is released by decohesion, and
- $f(\beta)$ is a function that enables us to parametrise the evolution of β in the decohesion process.

The state laws are deduced by applying (12) to (14):

$$\begin{cases} -(r_{\mathrm{N}}^{\mathsf{r}} + \beta\sigma_c) \in \partial \mathcal{I}_{\mathbb{R}_+}(u_{\mathrm{N}}), \\ -(A^{\mathsf{r}} + \sigma_c u_{\mathrm{N}} + w f'(\beta)) \in \partial \mathcal{I}_{[0,1]}(\beta). \end{cases} \tag{15}$$

The first law in (15) is a shifted Signorini condition by the value of the cohesive force defined by $r_{\mathrm{N}}^{\mathsf{c}}(\beta) = \beta\sigma_c$. This can be written in terms of a complementarity relation:

$$0 \leqslant r_{\mathrm{N}}^{\mathsf{r}} + r_{\mathrm{N}}^{\mathsf{c}}(\beta) \perp u_{\mathrm{N}} \geqslant 0. \tag{16}$$

The surface free energy Ψ_s is not a convex function of its arguments (u_{N},β) since the determinant of its Hessian matrix is equal to $-{\sigma_c}^2$. Nevertheless Ψ_s is convex with to respect to u_{N} since it is linear. By choosing $f'(\beta) \geqslant 0$, the convexity with respect to β is ensured. The smooth part of the free energy in (14) is composed of two terms. The first term $\beta\sigma_c u_{\mathrm{N}}$ is homogeneous to a potential energy given by the cohesive force $\beta\sigma_c$ in the displacement field u_{N}. The second term $w f(\beta)$ is the surface free energy released by decohesion for a given β. Some further modelling assumptions may also be specified on the function f. For an intact interface ($\beta = 1$), we may assume that $f(1) = 0$ such that the released free energy vanishes. For a broken interface ($\beta = 0$), we may assume that the cohesive free energy w has completely been released then $f(0) = 1$. Furthermore, we may also assume a monotone release for the cohesion free energy with β, that $f'(\beta) \leqslant 0$. This choice is consistent with the convexity of f if the minimum is attained for $\beta = 1$. In the following, these assumptions will be satisfied by the triangle law we propose.

Dissipation pseudo-potential and irreversible processes. To define the irreversibility of the process of decohesion in a way consistent with the second law of thermodynamics, the dissipation function, defined for an isothermal process as

$$\mathcal{D} = -\mathcal{P}_{\mathsf{int}} - \int_\Omega \dot{\Psi}\,\mathrm{d}x \tag{17}$$

must be non-negative. The computation of the time derivative of the non-smooth and non-convex potential requires some care. Assuming $\dot{\Psi}$ is convex in u_{N} and in β separately, a result in Frémond (2002, Appendix A.1.9) provides us with the following inequality:

$$\dot{\Psi}_s(u_{\mathrm{N}}, \beta) \leqslant -r_{\mathrm{N}}^{\mathsf{r}}\dot{u}_{\mathrm{N}} - A^{\mathsf{r}}\dot{\beta}, \tag{18}$$

for any $r_{\mathrm{N}}^{\mathsf{r}}$ and $\dot{\beta}$ that satisfies the inclusions (15)[1]. Substituting this inequality in the definition of the dissipation yields,

$$\mathcal{D} \geqslant \int_\Omega \boldsymbol{\sigma} : \dot{\boldsymbol{\varepsilon}}\,\mathrm{d}x - \int_\Gamma \left(v_{\mathrm{N}}^\top r_{\mathrm{N}} + \dot{\beta}A\right)\mathrm{d}x - \int_\Omega \frac{\partial \Psi_e(\varepsilon)}{\partial \varepsilon}\dot{\varepsilon}\,\mathrm{d}x + \int_\Gamma r_{\mathrm{N}}^{\mathsf{r}}\dot{u}_{\mathrm{N}} + A^{\mathsf{r}}\dot{\beta}\,\mathrm{d}x. \tag{19}$$

In (19), the terms integrated over Ω cancel out. We then obtain

$$\mathcal{D} \geqslant \int_\Gamma -v_{\mathrm{N}}^\top r_{\mathrm{N}} - \dot{\beta}A + v_{\mathrm{N}}^\top r_{\mathrm{N}}^{\mathsf{r}} + \dot{\beta}A^{\mathsf{r}}\,\mathrm{d}x. \tag{20}$$

Since we want to ensure that $\mathcal{D} \geqslant 0$, we will assume that

$$-v_{\mathrm{N}}^\top r_{\mathrm{N}} - \dot{\beta}A + v_{\mathrm{N}}^\top r_{\mathrm{N}}^{\mathsf{r}} + \dot{\beta}A^{\mathsf{r}} \geqslant 0, \text{ or equivalently, } -v_{\mathrm{N}}^\top r_{\mathrm{N}}^{\mathsf{ir}} - \dot{\beta}A^{\mathsf{ir}} \geqslant 0, \tag{21}$$

using the standard decomposition $r_{\mathrm{N}} = r_{\mathrm{N}}^{\mathsf{r}} + r_{\mathrm{N}}^{\mathsf{ir}}$ and $A = A^{\mathsf{r}} + A^{\mathsf{ir}}$ for the irreversible parts of the stress–like variables. A standard way to ensure this inequality is to postulate the existence of a proper closed convex pseudo-potential[2] of dissipation $\Phi(v_{\mathrm{N}}, \dot{\beta})$ such that the dissipation process is governed by

$$\begin{cases} -r_{\mathrm{N}}^{\mathsf{ir}} \in \partial_{v_{\mathrm{N}}}\Phi(v_{\mathrm{N}}, \dot{\beta}), \\ -A^{\mathsf{ir}} \in \partial_{\dot{\beta}}\Phi(v_{\mathrm{N}}, \dot{\beta}). \end{cases} \tag{22}$$

Let us assume that the dissipation process is only governed by the rate of β. We can choose for the pseudo potential of dissipation

$$\Phi(v_{\mathrm{N}}, \dot{\beta}) = \mathcal{I}_{\mathbb{R}_-}(\dot{\beta}). \tag{23}$$

This model of dissipation only imposes that the evolution of β must decrease with time, *i.e.*, $\dot{\beta} \leqslant 0$. The dissipative laws are thus

$$\begin{cases} -r_{\mathrm{N}}^{\mathsf{ir}} = 0, \\ -A^{\mathsf{ir}} \in \partial\mathcal{I}_{\mathbb{R}_-}(\dot{\beta}). \end{cases} \tag{24}$$

Equivalently, the last line of (24) can be written as

$$\dot{\beta} \in \partial\mathcal{I}_{\mathbb{R}_+}(-A^{\mathsf{ir}}). \tag{25}$$

In this form, we can easily interpret that A^{ir} is the force that drives the evolution of $\dot{\beta}$. Given that in (8), $A = 0$, we must have $A^{\mathsf{r}} = -A^{\mathsf{ir}}$, and thus

$$\dot{\beta} \in \partial\mathcal{I}_{\mathbb{R}_+}(A^{\mathsf{r}}). \tag{26}$$

Remark 1. *The choice of the pseudo potential* (23) *results in a model that is rate independent. A rate dependency can be easily added here by considering a model that is non-linear in the rates of the dissipative variables, such as*

$$\Phi(v_{\mathrm{N}}, \dot{\beta}) = \frac{c}{p+1}(-\dot{\beta})^{p+1} + \mathcal{I}_{\mathbb{R}_-}(\dot{\beta}), \tag{27}$$

where the coefficient c is a viscosity and p a given parameter for the nonlinear viscosity (Acary and Monerie, 2006).

Complete extrinsic cohesive zone model. Noting that $r_{\mathrm{N}} = r_{\mathrm{N}}^{\mathsf{r}}$, the complete model of the interface is given by

$$\begin{cases} \dot{\beta} \in \partial\mathcal{I}_{\mathbb{R}_+}(A^{\mathsf{r}}), \\ -(r_{\mathrm{N}} + \beta\sigma_c) \in \partial\mathcal{I}_{\mathbb{R}_+}(u_{\mathrm{N}}), \\ -(wf'(\beta) + \sigma_c u_{\mathrm{N}} + A^{\mathsf{r}}) \in \partial\mathcal{I}_{[0,1]}(\beta). \end{cases} \tag{28}$$

We highlight that as $r_{\mathrm{N}}^{\mathsf{ir}} = 0$ and (26) implies one of $\dot{\beta}$ or A^{r} is always zero, (21) is also zero. While the process of decohesion and surface creation is irreversible, it is also non-dissipative.

[1] The functions $u_{\mathrm{N}}(t)$ and $\beta(t)$ are assumed to be absolutely continuous, and hence they have a derivative almost everywhere, but not necessarily at any points. However, the inequality (18) can be obtained for the left and right time derivatives.

[2] a closed convex function is a convex function that is lower-semi continuous, or equivalently its epigraph is a closed convex set

Variational inequality and complementarity problem. The system can be formulated as an evolution variational inequality by

$$-F(\dot\beta,\beta,u_{\text{N}},r_{\text{N}},A^{\text{r}})\in \text{N}_{\mathbb{R}_+\times[0,1]\times\mathbb{R}_+}\left(\begin{bmatrix}u_{\text{N}}\\ \beta\\ A^{\text{r}}\end{bmatrix}\right),\ \text{with } F(\dot\beta,\beta,u_{\text{N}},r_{\text{N}},A^{\text{r}})=\begin{bmatrix}-\dot\beta\\ r_{\text{N}}+\beta\sigma_c\\ wf'(\beta)+\sigma_c u_{\text{N}}+A^{\text{r}}\end{bmatrix}. \tag{29}$$

Introducing slack variables μ, λ, and ν, this system can also be formalised using normal cones to convex sets as

$$\begin{cases}\dot\beta=-\lambda,\quad wf'(\beta)+\sigma_c u_{\text{N}}+A^{\text{r}}=\mu,\quad r_{\text{N}}+\beta\sigma_c=\nu,\\ -\nu\in\text{N}_{\mathbb{R}_+}(u_{\text{N}}),\quad -\mu\in\text{N}_{[0,1]}(\beta),\quad -\lambda\in\text{N}_{\mathbb{R}_+}(A^{\text{r}}).\end{cases} \tag{30}$$

Using the definition of a normal to a convex set defined by simple bounds, this model can be written with complementarity conditions as a Mixed Complementarity Systems (MCS)

$$\begin{cases}\dot\beta=-\lambda,\quad wf'(\beta)+\sigma_c u_{\text{N}}+A^{\text{r}}=\mu,\quad r_{\text{N}}+\beta\sigma_c=\nu,\quad \mu=\mu_+-\mu_-,\\ 0\leqslant\nu\perp u_{\text{N}}\geqslant 0,\quad 0\leqslant\mu_+\perp\beta\geqslant 0,\quad 0\leqslant\mu_-\perp 1-\beta\geqslant 0,\quad 0\leqslant\lambda\perp A^{\text{r}}\geqslant 0.\end{cases} \tag{31}$$

2.3 A linear evolution of the cohesion: triangle law.

We now specify the exact form of the surface potential. We require that when the surface doesn't exist, *i.e.* $u_{\text{N}}=0$ and $\beta=1$, $\Psi_s=0$, and that when the surface is fully decohered, *i.e.* $\beta=0$, $\Psi_s=w$. We assume that this decohesion is complete at a critical length $\delta_c>0$. Choosing

$$\begin{cases}w=\dfrac{\sigma_c\delta_c}{2},\\ f(\beta)=(\beta-1)^2,\end{cases} \tag{32}$$

fulfills the required conditions for the energy while ensuring that the potential remains convex in β. While $\beta\in[0,1]$ and $\dot\beta<0$, the second term in (31) gives $\beta=1-\dfrac{u_{\text{N}}}{\delta_c}$. The linear evolution of β, obtained as a consequence of (32), is depicted in Figure 1.

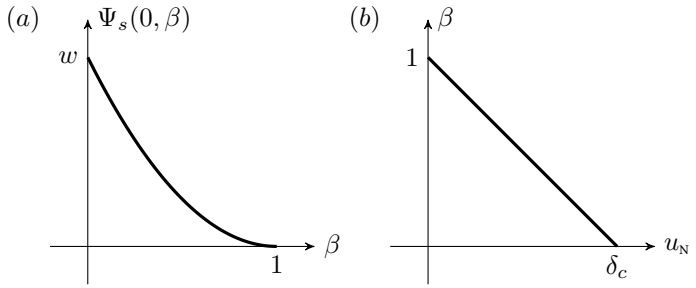

Figure 1: (a) The shape of the surface potential Ψ_s with respect to β. (b) The consequent linear evolution of β with u_{N}.

The model (30) is now specified for a triangle law by

$$\begin{cases}\dot\beta=-\lambda,\quad \sigma_c(\delta_c(\beta-1)+u_{\text{N}})+A^{\text{r}}=\mu,\quad r_{\text{N}}+\beta\sigma_c=\nu,\\ -\nu\in\text{N}_{\mathbb{R}_+}(u_{\text{N}}),\quad -\mu\in\text{N}_{[0,1]}(\beta),\quad -\lambda\in\text{N}_{\mathbb{R}_+}(A^{\text{r}}).\end{cases} \tag{33}$$

Since $\dot\beta$ is constrained to be non-positive, a smooth evolution of β starting with the initial value $\beta=1$ will result in β being less than 1. We will show that in this case the μ_- condition written in (31) is redundant and can be dropped from the formulation. Let us assume that $\beta=1$ and $\mu_->0$. As $\beta>0$, $\mu_+=0$ and $\mu=-\mu_-$. The second equation of (30) is then

$$\sigma_c u_{\text{N}}+A^{\text{r}}=-\mu_-. \tag{34}$$

As A^{r} and u_{N} are both constrained to be positive, (34) implies that $\mu_-\leqslant 0$, which contradicts our assumption. We conclude that μ_- vanishes. Thus, the condition is redundant and is dropped from the model in the following, allowing us to write $\mu=\mu_+$ and $-\mu\in N_{\mathbb{R}_+}(\beta)$.

This model in (33) can be written as a Mixed Linear Complementarity Systems (MLCS) given by

$$\begin{cases}\dot\beta=-\lambda,\quad \sigma_c(\delta_c(\beta-1)+u_{\text{N}})+A^{\text{r}}=\mu,\quad r_{\text{N}}+\beta\sigma_c=\nu,\\ 0\leqslant\nu\perp u_{\text{N}}\geqslant 0,\quad 0\leqslant\mu\perp\beta\geqslant 0,\quad 0\leqslant\lambda\perp A^{\text{r}}\geqslant 0.\end{cases} \tag{35}$$

Analytical expressions for an experiment with a given driven displacement Let us assume for a while that u_{N} is a given function of time t given by the following piecewise linear function:

$$u_{\mathrm{N}}(t) = \begin{cases} \frac{1}{2}t & \text{for } 0 \leqslant t \leqslant 1.0, \\ 1.0 - \frac{1}{2}t & \text{for } 1.0 \leqslant t \leqslant 2.0, \\ -1.0 + \frac{1}{2}t & \text{for } 2.0 \leqslant t, \end{cases} \tag{36}$$

and we choose $\delta_c = 1$ and $\sigma_c = \dfrac{1}{2}$. The time integration of the model described in (35) leads to the following piecewise linear response. We assume that the evolution is continuous.

- *First loading phase* $0 \leqslant t \leqslant 1.0$
  Since $u_{\mathrm{N}}(t) > 0$ for $t > 0$, the reaction force is $r_{\mathrm{N}} = -\beta\sigma_c$. Let us assume that $\beta(t) > 0$ for $t \in [0, T_1)$. We deduce that $\mu(t) = 0$. Let us note that $A^{\mathrm{r}}(t_0) = -\sigma_c(\delta_c(\beta_0 - 1) + u_{\mathrm{N}}(0)) = 0$. Let us assume that $\lambda(t) = 0, t \in [0, \varepsilon], \varepsilon > 0$ or equivalently $\dot{\beta}(t) = 0, t \in [0, \varepsilon], \varepsilon > 0$. In that case, we get $\dot{A}^{\mathrm{r}}(t) = -\sigma_c \dot{u}_{\mathrm{N}}(t) < 0$ and then $A^{\mathrm{r}}(\varepsilon) < 0$, for $\varepsilon > 0$ which is impossible. Let us try with $\dot{\beta}(t) < 0$, then $A^{\mathrm{r}}(t) = 0$ and $\beta(t) = 1 - \dfrac{u_{\mathrm{N}}(t)}{\delta_c}$ and $\dot{\beta}(t) = -\dfrac{\dot{u}_{\mathrm{N}}(t)}{\delta_c} < 0$. Since $\beta(1) = 1 - \dfrac{1}{2\delta_c} = \dfrac{1}{2} > 0$, this is the only consistent solution for $t \in [0, 1]$.

- *Unloading phase* $1 \leqslant t \leqslant 2$
  Let us assume that $\beta(t) > 0$ for $t \in [T_1, T_2)$ and $\mu(t) = 0$. Let us assume that $\lambda(t) = 0, t \in [0, \varepsilon], \varepsilon > 0$ or equivalently $\dot{\beta} = 0$. In that case, we get $\dot{A}^{\mathrm{r}}(t) = -\sigma_c \dot{u}_{\mathrm{N}}(t) > 0$ and then $A^{\mathrm{r}}(t) = \dfrac{1}{4}(t-1) > 0$. This solution satisfies the complementarity condition up to $t = 2$.

- *Second loading phase* $2 \leqslant t$
  Let us assume that $\beta(t) > 0$ for $t \in [T_1, T_2)$ and $\mu(t) = 0$. Let us assume that $\lambda(t) = 0, t \in [0, \varepsilon], \varepsilon > 0$ or equivalently $\dot{\beta} = 0$. In that case, we get $\dot{A}^{\mathrm{r}}(t) = -\sigma_c \dot{u}_{\mathrm{N}}(t) < 0$ and then $A^{\mathrm{r}}(t) = -\dfrac{1}{2}\sigma_c(t-2) + A^{\mathrm{r}}(2) = -\dfrac{1}{4}((t-3))$ which is positive for $t < 3.0$. For $t > 3.0$, the only possible solution of the complementarity leads to $\dot{\beta}(t) = -\dfrac{\dot{u}_{\mathrm{N}}(t)}{\delta_c} < 0$ and $A^{\mathrm{r}}(t) = 0$. The cohesion variable β is then $\beta(t) = -\dfrac{1}{2}(t-3) + \dfrac{1}{2}$ which is positive for $t < 4$. For $t > 4$, the solution is $\beta(t) = 0$ and $\mu(t) = \dfrac{1}{2}(u_{\mathrm{N}}(t) - 1)$

The solution of this experiment is depicted in Figure 2 with $\sigma_c = \dfrac{1}{2}$ and $\delta_c = 1$.

Remark 2. *Let us note that we need to derive the second term of* (35) *to get a closed form solution. This means that the evolution variational inequality is of relative degree at least* 1.

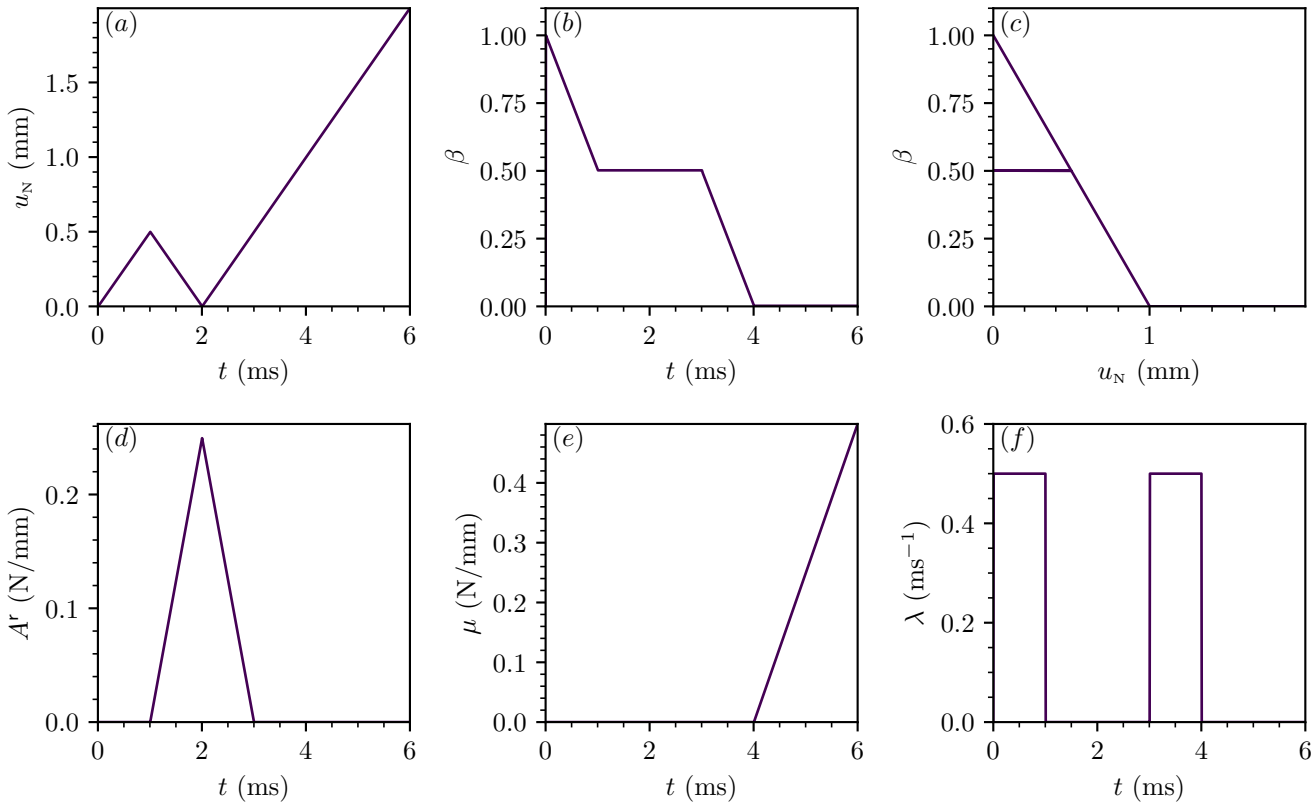

Figure 2: Illustration of the extrinsic cohesize law with a linear evolution of cohesion. We depict both the analytical solution derived above, and a numerical solution obtained by integrating a discretised form given in Section **??**. (a) The displacement u_N as a function of time t. (b) The cohesion β as a function of time t. (c) The cohesion β as a function of displacement u_N. (d) The thermodynamic driving force A^r as a function of time. (e) The slack variable μ as a function of time t. (f) The slack variable λ as a function of time t.

We observe in Figure 2 that the model behaves correctly, with β only changing as the crack opens $\dot{u}_N > 0$, and no change in β during reloading until u_N exceeds its previous maximum value. Once the interface cohesion is fully eliminated we observe no further change in β.

Remark 3. *Other types of smoother cohesion evolution behaviours are possible, for examples laws modelled after that proposed in Michel and Suquet (1994).*

3 Nonsmooth elasto–dynamics of finite dimensional systems

3.1 Finite dimensional systems via space discretisation

Let us consider a finite-dimensional model of a elastic linear mechanical system, potentially after a space discretisation by FEM. Let us note by $u \in \mathbb{R}^n$ the displacements of the system and $v = \dot{u}$ the velocity. Starting from the principle of virtual power (7), the equilibrium equation can be written as

$$M\dot{v} + K\,u = F; \quad \dot{u} = v \tag{37}$$

where $M \in \mathbb{R}^{n\times n}$ is the mass matrix, assumed to be symmetric positive definite, $K \in \mathbb{R}^{n\times n}$ is the structural stiffness matrix and $F \in \mathbb{R}^n$ is the external applied force.

Let us now add that the cohesive zone is applied on a finite set of cohesive contact points labelled by $\alpha \in [\![1, m]\!]$. In the case of small perturbations, the local displacements at contact $u_N = \mathrm{col}(\mathrm{u}_N^\alpha, \alpha \in [\![1, \mathrm{m}]\!])$ are related to the displacements u by a linear relation written as

$$u_N = Hu + b \tag{38}$$

where $H \in \mathbb{R}^{m\times n}$ and $b \in \mathbb{R}^m$. Collecting all variables at contact in the same way ($x = \mathrm{col}(x^\alpha, \alpha \in [\![1, m]\!])$), the equilibrium equations of the system are given by

$$\begin{cases} M\dot{v} + Ku = F + H^\top r_{\mathrm{N}}, \quad \dot{u} = v, \quad \dot{\beta} = -\lambda, \\ u_{\mathrm{N}} = Hu + b, \quad r_{\mathrm{N}}^{\mathsf{c}} = \sigma_c S\beta, \\ wf'(\beta) + \sigma_c u_{\mathrm{N}} + A^{\mathsf{r}} = \mu, \quad r_{\mathrm{N}} + r_{\mathrm{N}}^{\mathsf{c}} = \nu, \\ -\nu \in \mathrm{N}_{\mathbb{R}_+}(u_{\mathrm{N}}), \quad -\mu \in \mathrm{N}_{\mathbb{R}_+}(\beta), \quad -\lambda \in \mathrm{N}_{\mathbb{R}_+}(A^{\mathsf{r}}). \end{cases} \tag{39}$$

where $S \in \mathbb{R}^{m\times m}$ is a diagonal matrix that contains the tributary area of each cohesive zone node after space discretisation of the interface. For the sake of simplicity, we assume that σ_c, w and f do not depend on α, but this can be straightforwardly extended.

3.2 Non-smooth dynamics and impacts

In the presence of unilateral contacts, solutions of finite-dimensional dynamical systems with a regular mass matrix (with finite masses associated with all degrees of freedom) exhibit jumps in velocities. In this context, the non-smooth dynamics must be carefully treated to obtain a consistent time-discretisation (Moreau, 1999). To this end, the equations of motion of a discrete (finite-dimensional) mechanical system, and the relation with contact variables are written in terms of differential measures by

$$\begin{cases} M\,\mathrm{d}v + Ku\,\mathrm{d}t = F\,\mathrm{d}t + H^\top\,\mathrm{d}i_{\mathrm{N}}, \\ \dot{u} = v, \end{cases} \tag{40}$$

where $\mathrm{d}v$ is the differential measure associated with the velocity v, assumed to be a bounded value function, $\mathrm{d}i_{\mathrm{N}}$ is the measure of the reaction at the contact.

For the cohesive zone model, several further assumptions are made:

- We assume that the reaction due to cohesion force $r_{\mathrm{N}}^{\mathsf{c}}$ is bounded. In other words, the corresponding impulse does not contain atoms (Dirac measures);
- We assume that β and A are absolutely continuous functions of time. Since the evolution of the cohesion variable is governed to the displacement u_{N} that is assumed to be absolutely continuous in time, we assume the same regularity for β and A.

The reaction at the contact can be then decomposed into the "contact impulse" $\mathrm{d}p$, and the contribution of the cohesive forces by

$$\mathrm{d}i_{\mathrm{N}} = \mathrm{d}p_{\mathrm{N}} - \sigma_c S\beta\,\mathrm{d}t \tag{41}$$

When the interface is completely broken, we want to retrieve a contact law with impact. We choose in this work Moreau's impact law

$$0 \leqslant \mathrm{d}p_{\mathrm{N}} \perp v_{\mathrm{N}}^+ + ev_{\mathrm{N}}^- \geqslant 0, \text{ if } u_{\mathrm{N}} \leqslant 0, \text{ else } \mathrm{d}p_{\mathrm{N}} = 0, \tag{42}$$

where e is the Newton coefficient of restitution. In terms of normal cone inclusion, this is equivalent to

$$-\mathrm{d}p_{\mathrm{N}} \in \mathrm{N}_{T(u_{\mathrm{N}})}(v_{\mathrm{N}}^+ + ev_{\mathrm{N}}^-), \text{ or equivalently, } -(\mathrm{d}i_{\mathrm{N}} + \sigma_c S\beta\,\mathrm{d}t) \in \mathrm{N}_{T(u_{\mathrm{N}})}(v_{\mathrm{N}}^+ + ev_{\mathrm{N}}^-), \tag{43}$$

Remark 4. *The inclusion $-\mathrm{d}p_{\mathrm{N}} \in \mathrm{N}_{T(u_{\mathrm{N}})}(v_{\mathrm{N}}^+ + ev_{\mathrm{N}}^-)$ deals with the impact and the constraints at the velocity level. When $u_{\mathrm{N}}(t) = 0$, this inclusion imposes that $v_{\mathrm{N}}^+(t) \geqslant 0$ and then $u_{\mathrm{N}}(t+\epsilon) \geqslant 0$ for $\epsilon > 0$. This results is formalized in Moreau's viability lemma (Moreau, 1999). The inequality $u_{\mathrm{N}} \geqslant 0$ is not explicitly written since it is satisfied if* (42) *is satisfied and $u_{\mathrm{N}}(t_0) \geqslant 0$.*

Thus, we can write the full set of equations for the system as

$$\begin{cases} M\,\mathrm{d}v + Ku\,\mathrm{d}t = F\,\mathrm{d}t + H^\top(\mathrm{d}p_{\mathrm{N}} - \sigma_c S\beta\,\mathrm{d}t), \quad \dot{u} = v, \quad \dot{\beta} = -\lambda, \\ u_{\mathrm{N}} = Hu + b, \quad v_{\mathrm{N}} = Hv, \quad wf'(\beta) + \sigma_c u_{\mathrm{N}} + A^{\mathsf{r}} = \mu, \\ -\mu \in \mathrm{N}_{\mathbb{R}_+}(\beta), \\ -\lambda \in \mathrm{N}_{\mathbb{R}_+}(A^{\mathsf{r}}), \\ -\mathrm{d}p_{\mathrm{N}} \in N_{T_{\mathbb{R}_+}(u_{\mathrm{N}})}(v_{\mathrm{N}}^+ + ev_{\mathrm{N}}^-), \end{cases} \tag{44}$$

In complementarity terms, we write the model as

$$\begin{cases} M\,\mathrm{d}v + Ku\,\mathrm{d}t = F\,\mathrm{d}t + H^\top S(\mathrm{d}p_{\mathrm{N}} - \sigma_c S\beta\,\mathrm{d}t), \\ \dot{u} = v, \\ \dot{\beta} = -\lambda, \\ u_{\mathrm{N}} = Hu + b, \\ v_{\mathrm{N}} = Hv, \\ wf'(\beta) + \sigma_c u_{\mathrm{N}} + A^{\mathsf{r}} = \mu, \\ 0 \leqslant \mu \perp \beta \geqslant 0, \\ 0 \leqslant A^{\mathsf{r}} \perp \lambda \geqslant 0, \\ 0 \leqslant \mathrm{d}p_{\mathrm{N}} \perp v_{\mathrm{N}}^+ + ev_{\mathrm{N}}^- \geqslant 0, \text{ if } u_{\mathrm{N}} \leqslant 0, \text{ else } \mathrm{d}p_{\mathrm{N}} = 0. \end{cases} \tag{45}$$

The formulation of the dynamics of the problem with impact and a cohesize zone model is rather different from what is proposed in Acary and Monerie (2006). In (44), the cohesion impulse measure $-\sigma_c S\beta\,\mathrm{d}t$ is assumed to have only a density with respect to the Lebesgue measure. Furthermore, it is decoupled from the contact impulse measure $\mathrm{d}p_{\mathrm{N}}$ in the formulation of the constitutive laws of the interface. In other words, the cohesive reaction force is driven by u_{N} and the contact impulse measure by $v_{\mathrm{N}}^+ + ev_{\mathrm{N}}^-$.

4 Numerical time integration

4.1 Principles of the time integration scheme

The time-integration scheme is based on the same principle as the Moreau-Jean scheme (Jean and Moreau, 1992; Moreau, 1999) for contact dynamics. For the impulsive terms, the measure of the time interval $(k, k+1]$ is kept as a primary unknown:

$$p_{\mathrm{N},k,k+1} \approx \mathrm{d}p_{\mathrm{N}}((k,k+1]) = \int_{(k,k+1]} \mathrm{d}p_{\mathrm{N}}, \quad i_{\mathrm{N},k,k+1} \approx \mathrm{d}i_{\mathrm{N}}((k,k+1]) = \int_{(k,k+1]} \mathrm{d}i_{\mathrm{N}}, \tag{46}$$

All the continuous or bounded value terms are approximated with a θ-method as

$$\int_{t_k}^{t_{k+1}} x(t)\,\mathrm{d}t \approx hx_{k+\theta} \tag{47}$$

using the notation $x_{k+\theta} = \theta x_k + (1-\theta)x_{k+1}$ with $\theta \in [0,1]$. For the cohesive reaction force that is assumed to be bounded, we have

$$\int_{(k,k+1]} \mathrm{d}i_{\mathrm{N}} = \int_{(k,k+1]} \mathrm{d}p_{\mathrm{N}} - \int_{t_k}^{t_{k+1}} \sigma_c S\beta\,\mathrm{d}t \tag{48}$$

that is approximated by

$$i_{\mathrm{N},k,k+1} = p_{\mathrm{N},k,k+1} - h\sigma_c S\beta_{k+\theta} \tag{49}$$

Following this principle, the time-stepping scheme is written as follows:

$$\begin{cases} M(v_{k+1} - v_k) + hKu_{k+\theta} = hF_{k+\theta} + H^\top S(-h\beta_{k+\theta}\sigma_c + p_{\mathrm{N},k,k+1}), \\ u_{k+1} = u_k + hv_{k+\theta}, \\ \beta_{k+1} - \beta_k = -h\lambda_{k+1}, \\ u_{\mathrm{N},k+1} = Hu_{k+1} + b_{k+1}, \\ v_{\mathrm{N},k+1} = Hv_{k+1}, \\ wf'(\beta_{k+1}) + \sigma_c u_{\mathrm{N},k+1} + {A^{\mathsf{r}}}_{k+1} = \mu_{k+1}, \\ 0 \leqslant \beta_{k+1} \perp \mu_{k+1} \geqslant 0, \\ 0 \leqslant {A^{\mathsf{r}}}_{k+1} \perp \lambda_{k+1} \geqslant 0, \\ 0 \leqslant p_{\mathrm{N},k,k+1} \perp v_{\mathrm{N},k+1} + ev_{\mathrm{N},k} \geqslant 0, \text{ if } \tilde{u}_{n,k} \leqslant 0 \end{cases} \tag{50}$$

A conditional statement determining whether contact occurs is defined by an approximation of the displacement usually defined as :

$$\tilde{u}_{n,k} = u_{\mathrm{N},k} + \frac{h}{2} v_{\mathrm{N},k}, \tag{51}$$

The problem (50) amounts to solving a special type of finite–dimensional variational inequality at each time-step, namely a Mixed Complementarity System.

Discrete LCP for the triangular law. The only nonlinear term in the formulation of the complementarity system is due to f'. In the following, we show that if f' is linear, the problem (50) reduces to a Linear Complementarity System $\mathrm{LCP}(L, s)$ defined by

$$\begin{cases} w = Lz + q \\ 0 \leqslant w \perp z \geqslant 0 \end{cases} \tag{52}$$

Substituting in the triangle law in (50), we finally obtain the discretisation:

$$\begin{cases} M(v_{k+1} - v_k) + hKu_{k+\theta} = hF_{k+\theta} + H^\top S(-h\beta_{k+\theta}\sigma_c + p_{\mathrm{N},k,k+1}), \\ u_{k+1} = u_k + hv_{k+\theta}, \\ \beta_{k+1} - \beta_k = -h\lambda_{k+1}, \\ u_{\mathrm{N},k+1} = Hu_{k+1} + b_{k+1}, \\ v_{\mathrm{N},k+1} = Hv_{k+1}, \\ \sigma_c\delta_c(\beta_{k+1} - 1) + \sigma_c u_{\mathrm{N},k+1} + {A^{\mathrm{r}}}_{k+1} = \mu_{k+1}, \\ 0 \leqslant \beta_{k+1} \perp \mu_{k+1} \geqslant 0, \\ 0 \leqslant {A^{\mathrm{r}}}_{k+1} \perp \lambda_{k+1} \geqslant 0, \\ 0 \leqslant p_{\mathrm{N},k,k+1} \perp v_{\mathrm{N},k+1} + ev_{\mathrm{N},k} \geqslant 0 \end{cases} \tag{53}$$

Now, if we expand the first line with the appropriate θ-method substitutions, we arrive at

$$M(v_{k+1} - v_k) + hK\left(u_k + h\theta\left[(1-\theta)v_k + \theta v_{k+1}\right]\right) = h\left[(1-\theta)F_k + \theta F_{k+1}\right] + H^\top\left(-h\left(\theta\beta_{k+1} + (1-\theta)\beta_k\right)S\sigma_c + p_{\mathrm{N},k,k+1}\right) \tag{54}$$

We denote the augmented mass matrix as $\hat{M} = M + h^2\theta^2 K$ and the free impulse (without the contribution of the cohesive zone model) $\hat{i}_{k,k+1} = Mv_k - hK\left(u_k + h\theta(1-\theta)v_k\right) + h\left[(1-\theta)F_k + \theta F_{k+1}\right]$. Thus, the velocities can be determined by

$$v_{k+1} = \hat{M}^{-1}\left[\hat{i}_{k,k+1} + H^\top\left[-h\left(\theta\beta_{k+1} + (1-\theta)\beta_k\right)S\sigma_c + p_{\mathrm{N},k,k+1}\right)\right]. \tag{55}$$

When necessary, we apply the boundary condition enforcement technique in §A, so that we modify the augmented mass matrix $\hat{M}$ and the free impulse $\hat{i}$ to take into account Dirichlet boundary condition.

In the case where the contact conditional statement is fulfilled, we can formulate an LCP with three variable pairs, (A, λ), (β, μ) and $(v_{\mathrm{N}}^+ + ev_{\mathrm{N}}^-, p_{\mathrm{N}})$, noting that the unusual formulation of the third variable pair is required by the complementarity condition. In the most general case of multiple cohesive zones with boundary conditions enforced, the $\mathrm{LCP}(L, q)$ with

$$L = \begin{bmatrix} \mathbf{0} & -I & \mathbf{0} \\ I & \sigma_c\delta_c I - h^2\theta^2{\sigma_c}^2 WS & -h\theta\sigma_c WS \\ \mathbf{0} & h\theta\sigma_c WS & W \end{bmatrix}, \text{ with } W = H\hat{M}^{-1}H^\top$$

$$q = \begin{bmatrix} \beta_k \\ -\sigma_c\delta_c\left(\beta_k - \mathbf{1}\right) - \sigma_c\left(u_{\mathrm{N},k} + h\left[(1-\theta)v_{\mathrm{N},k} + \theta H\hat{M}^{-1}\left(\hat{i}_{k,k+1} - h(1-\theta)\sigma_c H^\top S\beta_k\right)\right]\right) \\ H\hat{M}^{-1}\left(\hat{i}_{k,k+1} - h(1-\theta)\sigma_c H^\top S\beta_k\right) + ev_{\mathrm{N},k} \end{bmatrix}, \tag{56}$$

is solved for the following variable

$$w = \begin{bmatrix} \beta_{k+1} \\ {A^{\mathrm{r}}}_{k+1} \\ v_{\mathrm{N},k+1} + ev_{\mathrm{N},k} \end{bmatrix}, \quad z = \begin{bmatrix} \mu_{k+1} \\ h\lambda_{k+1} \\ p_{\mathrm{N},k,k+1} \end{bmatrix}, \tag{57}$$

where $\mathbf{0}$ represents a matrix of zeroes, $\mathbf{1}$ represents a vector of ones, I is the identity matrix, and all of the cohesive zone variables should be understood as vectors. The choice of $h\lambda_{k+1}$ as an unknown of the LCP, rather than λ_{k+1}, is made to ensure L does not degenerate in the limit $h \to 0$. It is possible to straightforwardly generalise to each cohesive zone possessing its own values of the material parameters, in which case the material parameters can be treated as vectors.

4.2 Well-posedness of the discrete LCP

Proposition 1. *For a sufficiently small time step $h > 0$, such that $\sigma_c\delta_c I - h^2\theta^2{\sigma_c}^2 WS$ is positive definite, the $\mathrm{LCP}(L, q)$ defined by (56) has a solution. The solution is unique for β_{k+1} and λ_{k+1} and $v_{\mathrm{N},k+1}$. For $\beta_k > 0$, the solution is also unique for ${A^{\mathrm{r}}}_{k+1}$ and μ_{k+1}.*

We start by proving that L is a semi-positive definite matrix for sufficiently small h. Proving this property for L amounts to proving that $\frac{1}{2}(L+L^\top)$ given by

$$\frac{1}{2}(L+L^\top)=\begin{bmatrix}\mathbf{0} & \mathbf{0} & \mathbf{0}\\ \mathbf{0} & \sigma_c\delta_c I-h^2\theta^2{\sigma_c}^2WS & \mathbf{0}\\ \mathbf{0} & \mathbf{0} & W\end{bmatrix}, \tag{58}$$

is also a semi-definite matrix. Since M is a positive definite matrix, the matrix $W=H\hat{M}^{-1}H^\top$ is a semi-positive definite matrix. Since $\sigma_c\delta_c I$ is a positive definite matrix, $\sigma_c\delta_c I-h^2\theta^2{\sigma_c}^2H\hat{M}^{-1}H^\top S$ is also a positive definite matrix for sufficiently small h. Therefore, we can conclude that L is a semi-definite positive matrix. From Theorem 3.1.2 in Cottle et al. (2009), if the $\mathrm{LCP}(L,s)$, with a semi-definite positive matrix, is feasible, then it is solvable. The feasibility conditions for a LCP are given by

$$Lz+q\geqslant 0 \text{ and } z\geqslant 0, \tag{59}$$

and in the case of $\mathrm{LCP}(L,q)$, we get

$$\begin{cases} z_1\geqslant 0, z_2\geqslant 0, z_3\geqslant 0,\\ -z_2+\beta_k\geqslant 0,\\ z_1+\left[\sigma_c\delta_c I-h^2\theta^2{\sigma_c}^2WS\right]z_2-h\theta\sigma_cWSz_3+q_2\geqslant 0,\\ h\theta\sigma_cWz_2+Wz_3+q_3\geqslant 0. \end{cases} \tag{60}$$

Rearranging the inequality, we obtain

$$\begin{cases} 0\leqslant z_2\leqslant \beta_k,\\ z_1\geqslant -\left[\sigma_c\delta_c I-h^2\theta^2{\sigma_c}^2W\right]z_2+h\theta\sigma_cWSz_3-q_2, z_1\geqslant 0,\\ Wz_3\geqslant -q_3-h\theta\sigma_cWz_2, z_3\geqslant 0. \end{cases} \tag{61}$$

Since $\beta_k\geqslant 0$, the first inequality is feasible for z_2. Let us search for a feasible point $z^\star$ such that $z_2^\star=0$. We must check that the following inequalities are feasible for $z_1^\star$ and $z_3^\star$:

$$\begin{cases} z_1^\star\geqslant h\theta\sigma_cWSz_3-q_2, z_1^\star\geqslant 0,\\ Wz_3^\star+q_3\geqslant 0, z_3^\star\geqslant 0. \end{cases} \tag{62}$$

Let us consider that $z_3^\star$ is the solution of the following quadratic program

$$\begin{aligned} \min_z \quad & \tfrac{1}{2}z_3^TWz_3+z_3^Tq_3,\\ & z_3\geqslant 0. \end{aligned} \tag{63}$$

Since W is a symmetric semi-definite positive matrix, such a point $z_3^\star$ exists and satisfies the optimality condition

$$Wz_3^\star+q_3\geqslant 0, z_3^\star\geqslant 0, (Wz_3^\star+q_3)^\top z_3^\star=0. \tag{64}$$

Finally, let us choose $z_1^\star=\max(0,h\theta\sigma_cWSz_3^\star-q_2)$, we have proved that the point $z=\mathrm{col}(z_1^\star,0,z_3^\star)$ is a feasible point of the inequalities (60). The $\mathrm{LCP}(L,q)$ is feasible and thus solvable.

For the uniqueness of the solution, we use the characterization of the solutions of $\mathrm{LCP}(L,q)$, denoted by $\mathrm{SOL}(L,q)$, when L is a semi-positive definite matrix (Cottle et al., 2009, Theorem 3.1.7) as a polyhedral set defined by

$$\mathrm{SOL}(L,q)=\{z\mid z\geqslant 0, Lz+q\geqslant 0, q^\top(z-\bar{z})=0, (L+L^\top)(z-\bar{z})=0\}, \tag{65}$$

where $\bar{z}$ is an arbitrary solution. In our case, the condition $(L+L^\top)(z-\bar{z})=0$ yields

$$\begin{cases} \left[\sigma_c\delta_c I-h^2\theta^2{\sigma_c}^2WS\right](z_2-\bar{z}_2)=0,\\ W(z_3-\bar{z}_3)=0. \end{cases} \tag{66}$$

Since $\sigma_c\delta_c I-h^2\theta^2{\sigma_c}^2WS$ has full-rank a sufficiently small h, we get that z_2, and hence $h\lambda_{k+1}$ is unique. Since $\beta_{k+1}=\beta_k-h\lambda_{k+1}$, β_{k+1} is also unique. From $w_3-\bar{w}_3=h\theta\sigma_cWS(z_2-\bar{z}_2)+W(z_3-\bar{z}_3)=0$, we conclude that w_3 is unique and therefore $v_{\mathrm{N},k+1}$ is also unique. Furthermore, $(z_3-\bar{z}_3)$ is in the kernel of $H^\top$, so we have also $H^\top(z_3-\bar{z}_3)=0$.

From the condition, $q^\top(z-\bar{z})=0$, we obtain

$$\beta_k(z_1-\bar{z}_1)+\left[H\hat{M}^{-1}\left(\hat{i}_{k,k+1}-h(1-\theta)\sigma_cH^\top S\beta_k\right)+ev_{\mathrm{N},k}\right]^T(z_3-\bar{z}_3)=0, \tag{67}$$

since $z_2 - \bar{z}_2 = 0$. Since $v_{\text{N},k} = Hv_k$, we have the following simplification

$$\left[\hat{M}^{-1}\left(\hat{i}_{k,k+1} - h(1-\theta)\sigma_c H^\top S\beta_k\right) + ev_k\right]^\top H^\top(z_3 - \bar{z}_3) = 0, \tag{68}$$

since $H^\top(z_3 - \bar{z}_3) = 0$ and then

$$\beta_k(z_1 - \bar{z}_1) = 0. \tag{69}$$

For $\beta_k > 0$, z_1, hence μ_{k+1} is unique. Using that the linear relations ${A^{\text{r}}}_{k+1} = \mu_{k+1} - \sigma_c\delta_c(\beta_{k+1} - 1) + \sigma_c u_{\text{N},k+1}$ and $u_{\text{N},k+1} = u_{\text{N},k} + hv_{\text{N},k+\theta}$, we conclude that ${A^{\text{r}}}_{k+1}$ is unique if $\beta_k > 0$.

Corollary 1. *The solution of the problem* (53) *exists and is unique for the variables* $(v_{k+1}, u_{k+1}, \beta_{k+1}, \lambda_{k+1})$ *for a sufficiently small time step* h.

The uniqueness of β_{k+1} comes from Proposition 1. For the uniqueness of v_{k+1}, let us consider two solutions $\hat{v}_{k+1}$ and $\bar{v}_{k+1}$, from (55), we get

$$\hat{v}_{k+1} - \bar{v}_{k+1} = \hat{M}^{-1}\left[H^\top\left[-h\left(\theta(\hat{\beta}_{k+1} - \bar{\beta}_{k+1}) + (1-\theta)\beta_k\right)S\sigma_c + (\hat{p}_{\text{N},k,k+1} - \bar{p}_{\text{N},k,k+1})\right)\right]. \tag{70}$$

Since $\hat{p}_{\text{N},k,k+1} - \bar{p}_{\text{N},k,k+1}$ is in the kernel of $H^\top$ and $\beta_{k+1} - \bar{\beta}_{k+1} = 0$, we can conclude that v_{k+1} is unique, and the integration rule $u_{k+1} = u_k + hv_{k+\theta}$ implies the uniqueness of u_{k+1}.

Remark 5. *The condition of the time-step is not a strong condition in practice since it is based on the condition that* $\sigma_c\delta_c I - h^2\theta^2{\sigma_c}^2 WS$ *is positive definite in which* h *only appears as* h^2. *In most finite elements applications,* H *is often assumed to be full-rank. In that case,* $p_{\text{N},k,k+1}$ *is also unique. The non-uniqueness of* μ_{k+1} *and* ${A^{\text{r}}}_{k+1}$ *when* $\beta_k = 0$ *comes from the fact that we impose two redundant constraints related to* $\beta \geqslant 0$ *and* $\dot{\beta} \leqslant 0$. *In practice, this is harmless since it does not influence the state variables* $(v_{k+1}, u_{k+1}, \beta_{k+1})$.

5 Numerical Validations

5.1 Quasi-static scalar case with elastic spring

For the sake of illustration, we will consider firstly a static system. Let us consider the case of an elastic rod bound onto a rigid substrate with a cohesive zone, as outlined in Acary and Monerie (2006) and Chaboche et al. (2001). First, we consider the structural stiffness matrix:

$$K = \begin{bmatrix} ES/\ell & -ES/\ell \\ -ES/\ell & ES/\ell \end{bmatrix}, \tag{71}$$

where ℓ is the rod length, S the rod cross-sectional area (and area of the cohesive zone) and E is the Young's modulus of the rod. However, it is clear that this matrix is singular, so we modify it (and the external force F) following §A, in order to enforce the boundary conditions and create an invertible matrix $\bar{K}$. If we consider (39) in static equilibrium (i.e. where we remove the Mv term from the equilibrium equation), we obtain an LCP $w = Lz + q \perp z$ from the fully implicit discretisation, where

$$w = \begin{bmatrix} \beta_{k+1} \\ {A^{\text{r}}}_{k+1} \\ u_{\text{N},k+1} \end{bmatrix}, \quad L = \begin{bmatrix} 0 & -1 & 0 \\ 1 & \sigma_c\delta_c - {\sigma_c}^2 H\bar{K}^{-1}H^\top S & -\sigma_c H\bar{K}^{-1}H^\top S \\ 0 & \sigma_c H\bar{K}^{-1}H^\top S & H\bar{K}^{-1}H^\top S \end{bmatrix}, \quad z = \begin{bmatrix} \mu_{k+1} \\ h\lambda_{k+1} \\ \nu_{k+1} \end{bmatrix}, \tag{72}$$

$$q = \begin{bmatrix} \beta_k \\ -\sigma_c\left(\delta_c(\beta_k - 1) + H\bar{K}^{-1}\left[\bar{F}_{k+1} - H^\top S\sigma_c\beta_k\right] + b\right) \\ H\bar{K}^{-1}\left(\bar{F}_{k+1} - H^\top S\sigma_c\beta_k\right) + b \end{bmatrix}. \tag{73}$$

We can then solve this system for the case where the far end of the rod is driven according to the relation

$$u_2(t) = \begin{cases} \frac{1}{2}t, & 0 \leqslant t < 1.0 \\ 1.0 - \frac{1}{2}t, & 1.0 \leqslant t < 3.0 \\ -2.0 + \frac{1}{2}t, & 3.0 \leqslant t \end{cases} \tag{74}$$

where extension is taken to be positive, and compression negative. The solution of the system (72) under driving input (74) with $H = \begin{bmatrix} 1 & 0 \end{bmatrix}$, material parameters $\sigma_c = 0.5$, $\delta_c = 1.0$, $E = 5.0$ and $\ell = 1.0$, and 4000 time-steps is given in Figure 3:

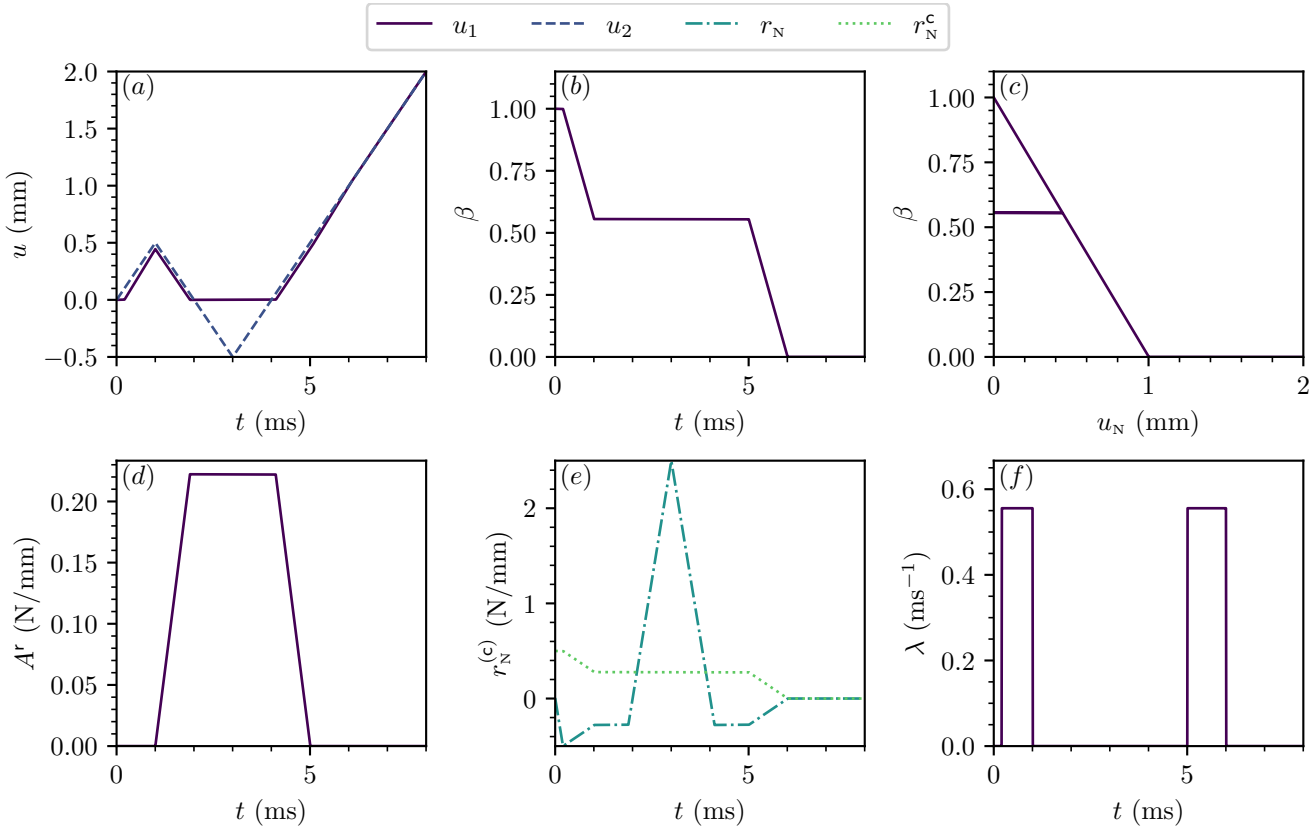

Figure 3: The solutions of the elastic bar with cohesive zone system. (a) The nodal displacements u_1 and u_2 as a function of time t. (b) The cohesion β as a function of time t. (c) The cohesion β as a function of crack opening displacement u_N. (d) The driving force A^r as a function o time t. (e) The reversible part of the reaction force r_N and the cohesive force r_N^c as a function of time t. (f) The rate of decohesion λ as a function of time t.

However, we must be careful that the behaviour of the system remains well-posed. When we have

$$\sigma_c \delta_c - H \bar{K}^{-1} H^\top S \leqslant 0, \tag{75}$$

the system loses uniqueness and multiple solutions are possible. So long as the condition

$$\sigma_c \delta_c > \frac{\ell}{E}, \tag{76}$$

is fulfilled, the system remains stable and there is a unique solution. Physically the unstable behaviour represents the accumulation of more elastic strain energy than can be released at the cohesive zone. For the sake of illustration, we simulate the above system, but with $E = 0.5$ in Figure 4:

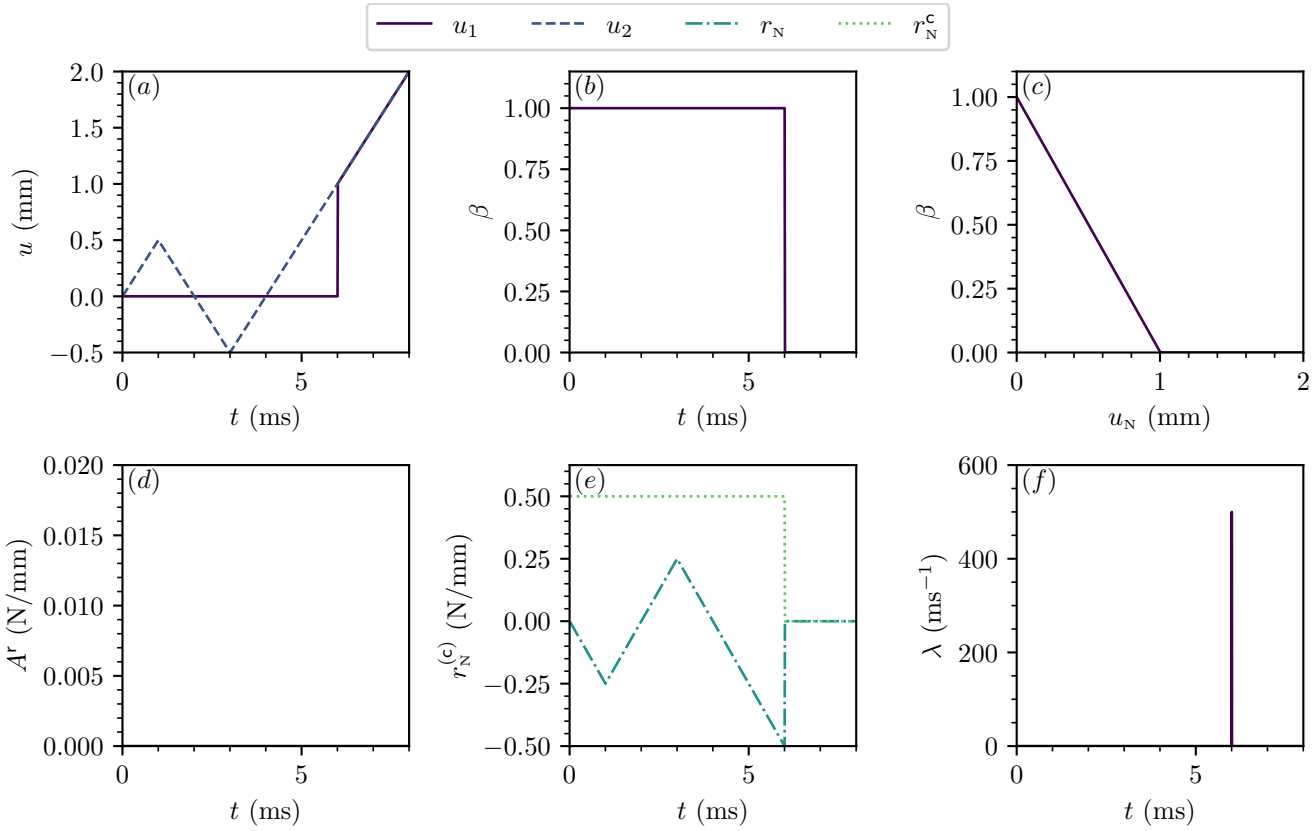

Figure 4: The solutions of the elastic bar with cohesive zone system for ill-posed system values. (a) The nodal displacements u_1 and u_2 as a function of time t. (b) The cohesion β as a function of time t. (c) The cohesion β as a function of crack opening displacement u_N. (d) The driving force A^r as a function o time t. (e) The reversible part of the reaction force r_N and the cohesive force r_N^c as a function of time t. (f) The rate of decohesion λ as a function of time t.

We may observe that the loss of uniqueness results in a "solution jump", where the system moves from completely unbroken to completely broken in a single time-step. Physically, this occurs because more energy is stored elastically than can be released by the cohesive zone, resulting in the instantaneous rupture once the critical traction is achieved. It should also be noted that if larger time-steps are chosen, the value of u_N at which β goes to zero are subject to "overshoot", meaning that an additional spurious energy release occurs.

This ill-posed system behaviour can be entirely avoided by working in dynamics, so from this point onwards we do so. However, as Figure 3 demonstrates, the model can be successfully implemented in statics, provided that (76) is always respected.

5.2 Dynamic cohesive zone model with elasticity

5.2.1 Dynamic case with single elastic spring

Now, we consider firstly the same system as above, but this time in dynamics. We use the system parameters $\sigma_c = 0.5$ MPa, $\delta_c = 1.0$ mm, $e = 0.0$, $E = 0.5$ MPa, $l = 1$ mm, $S = 1$ mm^2, and $M = \begin{bmatrix} 0.25 & 0 \\ 0 & 0.25 \end{bmatrix}$ g. These values result in an ill-posed system in the static case, but as we demonstrate below, the addition of dynamics regularises the system. We simulate the system for 8 ms using 4000 time-steps and $\theta = 1$, subject to the same driving displacement (74). We observe the system evolution depicted in Figure 5:

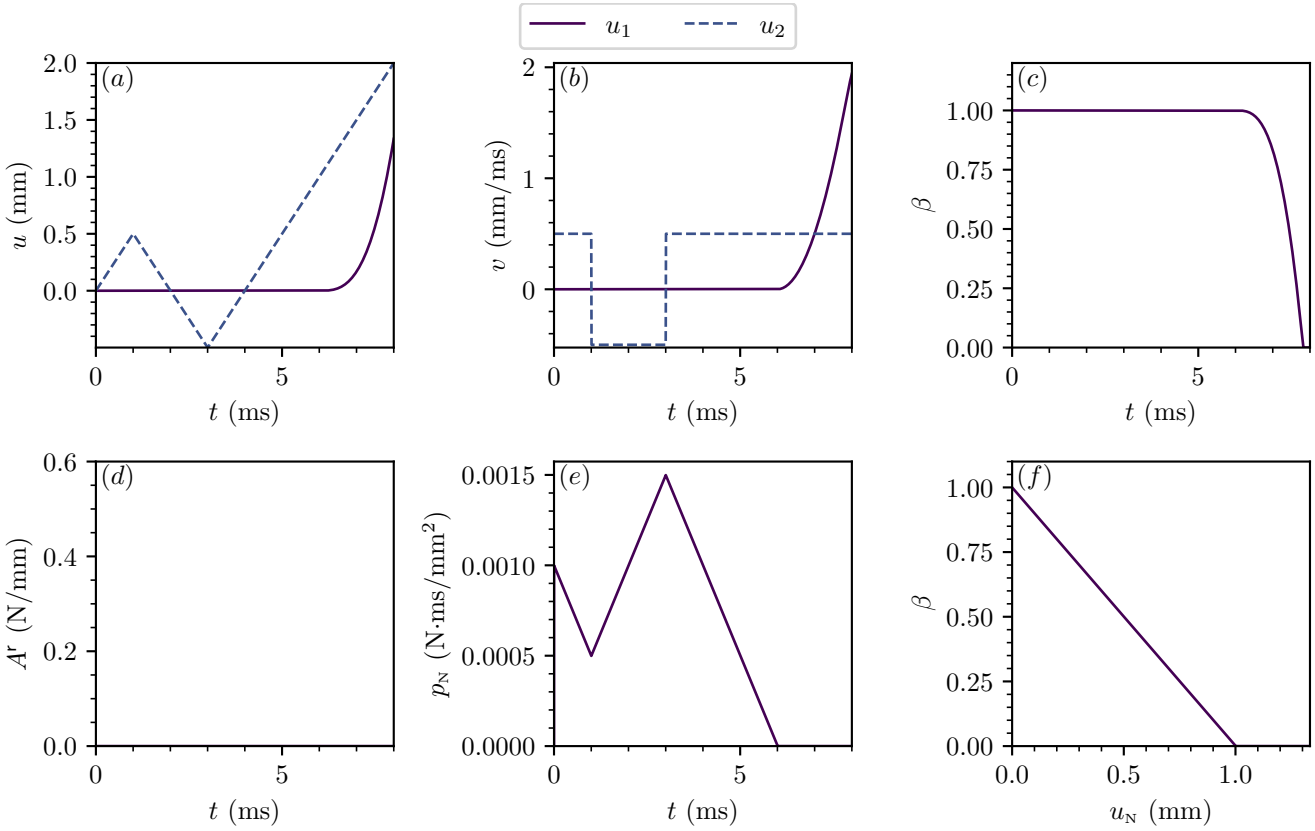

Figure 5: The solutions of the dynamic CZM system with elasticity, for values that are ill-posed in statics. (a) The driving force F as a function of time t. (b) The displacements u as a function of time t. (c) The velocities v as a function of time t. (d) The cohesion β as a function of time t. (e) The thermodynamic force A^{r} as a function of time t. (f) The percussion p_{N} as a function of time t.

We may observe in Figure 5 that the inertial effects result in a smoothly changing value of β with time, as opposed to the instantaneous rupture of the equivalent system in statics, thus demonstrating the well-posed nature of the system.

5.2.2 Dynamic Double Cantilever Beam

In order to simulate a double cantilever beam (DCB), we apply the boundary condition enforcement technique in §A. In the case where we have more than one node with a cohesive zone, the possibility arises that some of the nodes fulfil the contact condition, while others do not. We simulate the system by first constructing the LCP assuming all points are in contact, and then creating submatrix L_{sub} and subvector s_{sub} from L and s by removing the entries corresponding to the $v_{\mathrm{N},k+1} + ev_{\mathrm{N},k}$ - $p_{\mathrm{N},k,k+1}$ variable pairs for the nodes not in contact. The w and z vectors are automatically re-sized, and the corresponding LCP $w = L_{\text{sub}}z + s_{\text{sub}}$ is solved. The values of the removed variables can then be updated by setting the corresponding $p_{\mathrm{N},k,k+1} = 0$ and updating the velocities via (55) and (50).

It is important to note that the LCP becomes infeasible if $\beta_k < 0$. While in principle the constraints act to enforce a $\beta_k = 0$ condition, in practice due to the finite numerical precision of the solution at each step, the condition can be violated. In this case, the solution of the LCP can fail in turn. As such, we take care to set any value of $\beta_{k+1} \leqslant 1 \times 10^{-12}$ to $\beta_{k+1} = 0$, and we remove the corresponding entries from the LCP for the next time step as described above for the non-contact entries. The corresponding value of μ_{k+1} that is also removed from the LCP is calculated instead from the expression in (50). We note that this schema is also effective numerically, as by decreasing the size of the LCP, we speed up its solution.

We simulate only half the system, exploiting the symmetry inherent to the problem. Thus, the lower boundary of the system consists of a series of nodes with cohesive zones attached, excepting a section representing an initial crack. It is important to note that where the Dirichlet boundary intersects with the cohesive zone boundary, the node is removed from the set of cohesive zone nodes, and its tributary area is allocated to the neighbouring cohesive node. Thus, the crack is allowed to propagate over the entire length of the system, but there is no possibility of the LCP being made infeasible by trying to enforce the Dirichlet boundary condition on a cohesive zone node.

We simulate a system inspired by that found in Camacho and Ortiz (1996), but using parameters for PMMA. We will simulate a double cantilever beam with a length of 2 mm, with a pre-existing crack of 0.4 mm length. The beam is taken to have a thickness of 1 mm. The bulk material has Young's modulus $E = 2.7 \times 10^3$ MPa, a Poisson's ratio $\nu = 0.39$ (Doitrand et al., 2021), and a mass density

$\rho = 1.18 \times 10^{-3}$ g/mm^3 (Doitrand et al., 2019). The cohesive zone parameters are the critical traction $\sigma_c = 45$ MPa, the fracture energy $G_c = 0.14$ N/mm, and the critical distance $\delta_c = 0.0062$ mm.

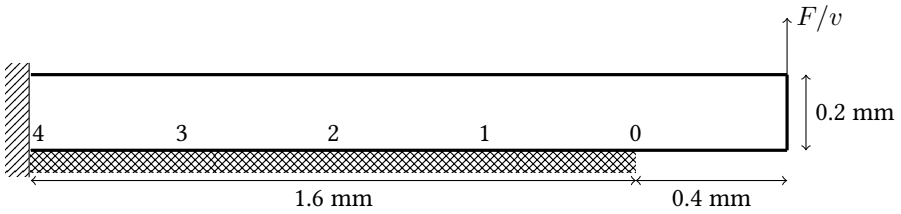

Figure 6: The symmetry of the DCB allows us to simulate it as a single cantilever beam fixed at the left end (diagonal hatching), with cohesive zone nodes attached to a rigid substrate along the symmetry plane. A force or velocity is applied at the upper right hand corner, at the free end. We follow the decohesion at the points labelled 0 through 4.

We simulate the upper half of the DCB shown in Figure 6 using a controlled displacement test, displacing at the rate of 1 mm/s to a target displacement at the free end of 0.6 mm. We adopt an initial step of $h = 1.2$ ms, with $\theta = 0.5$. However, this step size is too large once the crack initiates, meaning that we adopt an adaptive time-stepping scheme such that if the LCP does not resolve correctly, the step size is halved and the step is attempted again, repeating until resolution is successful. If ten steps in a row are successfully completed, the step size is multiplied by 1.5. This schema ensures sufficiently fine temporal resolution while maintaining computational efficiency. The results of the simulation are shown in Figure 7:

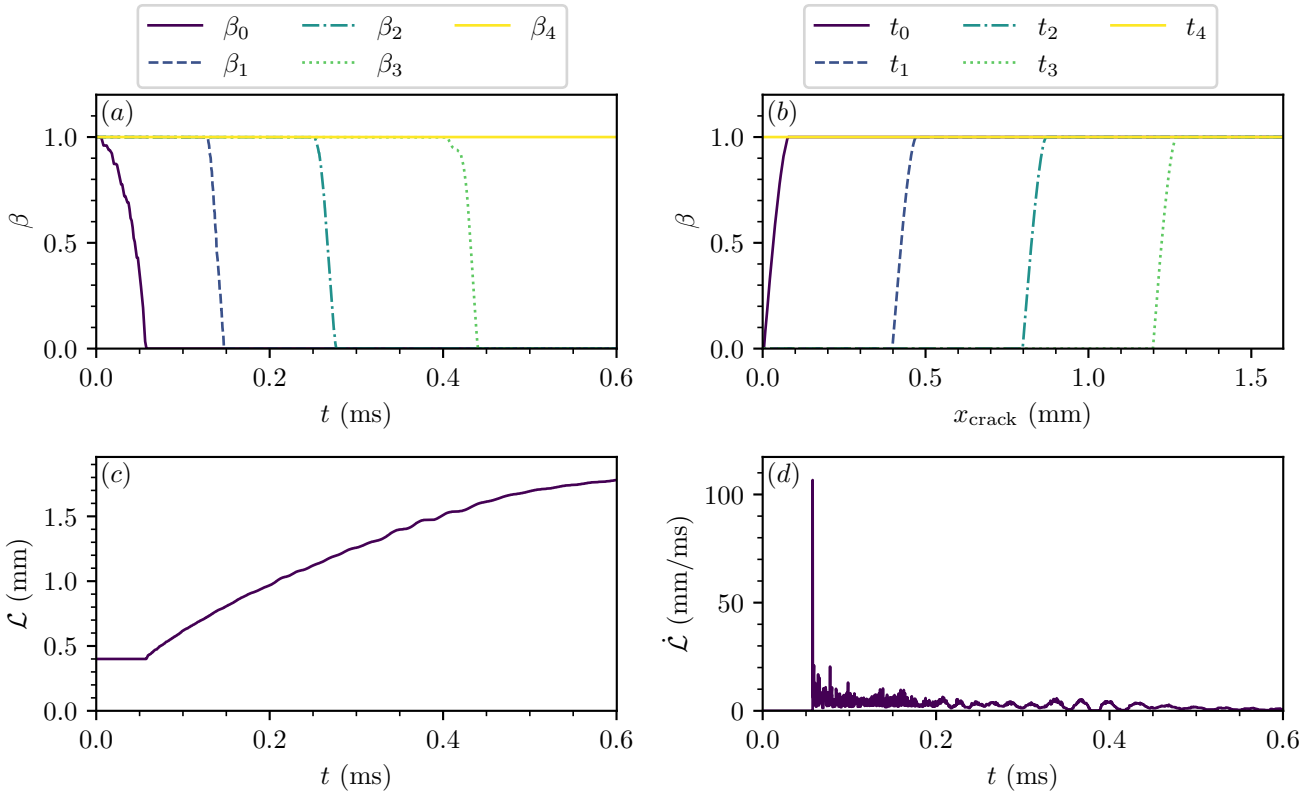

Figure 7: The simulation of a double cantilever beam under velocity control. (a) The cohesion β as a function of time t at the points of interest. (b) The cohesion β as a function of distance from the tip of the initial crack x_{crack}, at the time that each of the points of interest goes to zero. (c) The length $\mathcal{L}$ of the crack as a function of time t. (d) The crack tip velocity $\dot{\mathcal{L}}$ as a function of time t.

The crack tip velocity is calculated by assuming a linear growth between each spatial point as they crack. We may observe in Figure 7 that the speed of the decohesion is relatively constant over time, other than for the very first point to crack, which takes substantially longer than the others. Some slowing of the initial decohesion is observable in the curve for β_3 in subfigure (a), as a result of the influence of the geometry of the problem. Similarly, in subfigure (b), we can see that the size of the fracture process zone remains essentially constant throughout the cracking process. Subfigures (c) and (d) demonstrate the relatively steady growth in the crack length, with an initial sharp increase occuring as the crack establishes before gradually tapering away.

We can also consider the energy-conserving properties of the integration scheme, by plotting the changing energetic quantities:

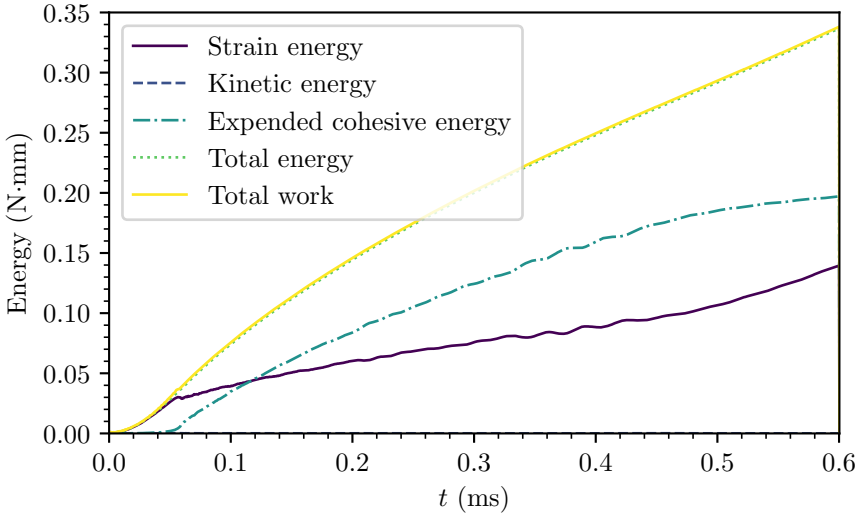

Figure 8: The energies of the dynamic double cantilever beam simulation under velocity control.

We can see in Figure 8, that the work input matches exactly with the sum of the strain, kinetic and expended cohesive energies, indicating that the integration scheme successfully conserves the energy. A comparatively greater share of the work input is used in the creation of new surface area (i.e. the expended cohesive energy) than in the storage of strain energy, while the kinetic energy remains negligible (as is to be expected in a slow displacement-controlled simulation).

We also simulate the same system under force control, this time increasing the loading according to $F = 10t$ N until one element is fully decohered, at which point the force is held constant. The simulation was terminated when 20 time-steps had passed with no changes to the value of β at any of the cohesive zone nodes. The results of the simulation are shown in Figure 9:

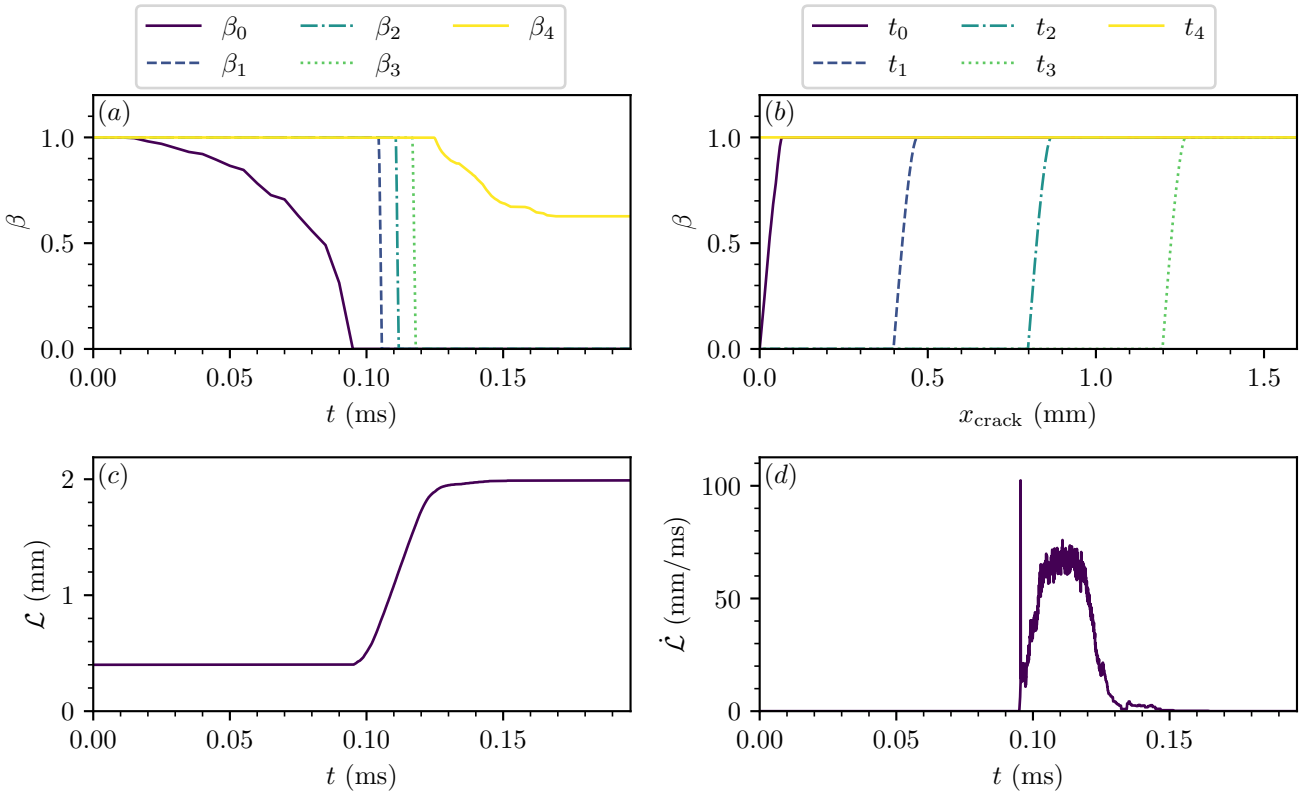

Figure 9: The simulation of a double cantilever beam under force control. (a) The cohesion β as a function of time t at the points of interest. (b) The cohesion β as a function of distance from the tip of the initial crack x_{crack}, at the time that each of the points of interest goes to zero. (c) The length $\mathcal{L}$ of the crack as a function of time t. (d) The crack tip velocity $\dot{\mathcal{L}}$ as a function of time t.

In comparing Figure 7 and Figure 9, we may observe that the force-controlled system decoheres much more slowly initially, up until the point at which the crack begins, where it then travels much more rapidly than the velocity-controlled system, with crack arrest being achieved by the interaction with the fixed boundary of the system. We note that the decohesion of points 1, 2 and 3 are more rapid and more concentrated in time than for the velocity controlled system, and that point 4 experiences some decohesion, whereas it remained intact for the velocity controlled system. Once again, we can also consider the energetic properties of the system:

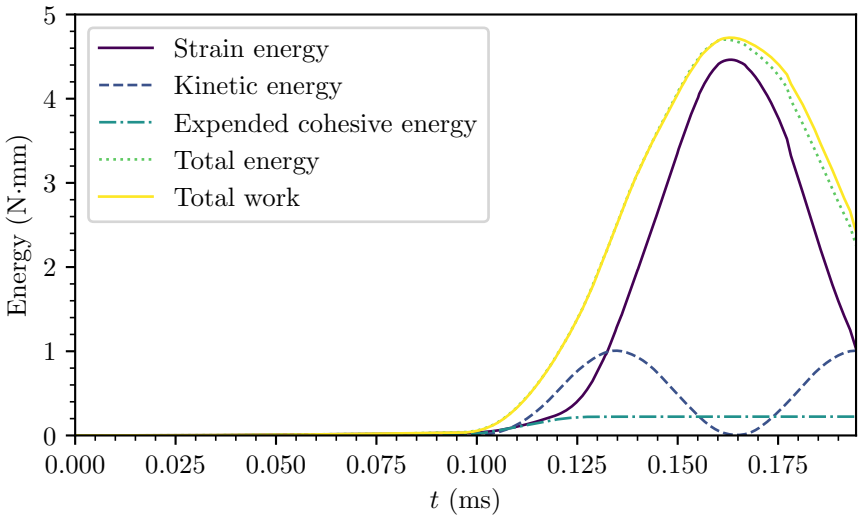

Figure 10: The energies of the dynamic double cantilever beam simulation under force control.

We may observe that the energetic behaviour of this system depicted in Figure 10 is rather different to that of the velocity controlled system. We observe that the system is truly dynamic, and a significant part of the work input is transformed into kinetic energy. We also observe that at a certain point, the work input decreases and the system moves towards its equilibrium state, with a certain amount of surface energy, and exchanges between the strain and kinetic energies. We note that the total system energy is slightly below that of the total work input once the work input begins to decrease, indicating some numerical dissipation due to our integration scheme.

5.2.3 Rhombus hole simulation

We can also simulate the rhombus hole specimen in Doitrand et al. (2019), applying (56) with the same principles as for the DCB. The sample has a width of 40 mm and a height of 60 mm, with a rhombus hole in the centre that has a corner angle of 90° and a half-diagonal length of 4.95 mm. While the simulation in Doitrand et al. (2019) is purely in two dimensions, we consider a three-dimensional system in plane-stress, and so use a thickness of 1 mm.

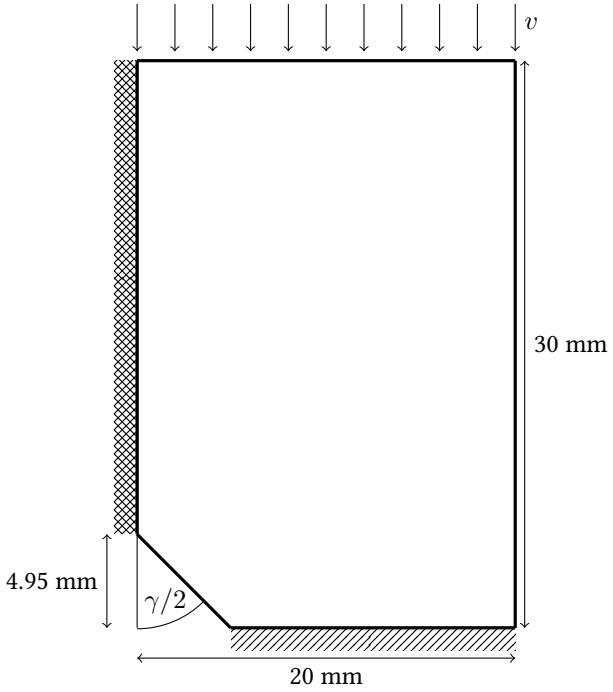

Figure 11: The double symmetry of the rhombus hole specimen allows us to simulate only the top right quarter. Standard symmetry conditions (diagonal hatching) are applied to the bottom boundary, while cohesive zone nodes and a symmetry condition are attached to the left boundary. A velocity is applied uniformly to all points on the top boundary. The vertical half diagonal retains a constant length, but the angle γ is varied to produce different geometries. I changed β to γ to avoid any confusion with the cohesion.

We exploit symmetry so that we need only simulate one quarter (the top-right) of the sample. The boundary conditions on the left and bottom edges are thus symmetry conditions, with normal displacements restricted to be positive or zero, and tangential displacements unrestrained. The right edge and the rhombus hole edge are similarly unrestrained, while the loading is applied as a Dirichlet condition on the top edge. As the crack is predicted to occur along the left edge, these nodes are included in the set of cohesive zone nodes. The 1 mm length closest to the corner of the rhombus hole is allocated a very fine mesh, with one node every 0.002 mm, ensuring accurate resolution of the cohesive zone. The mesh is steadily coarsened to reach a characteristic size of 0.5 mm at the top of the left hand edge, while all of the bulk regions that exhibit purely elastic behaviour are allocated a characteristic size of 2 mm. Hence, the mesh is highly refined in the region of the crack process, while remaining computationally efficient. The mesh is shown in Figure 12:

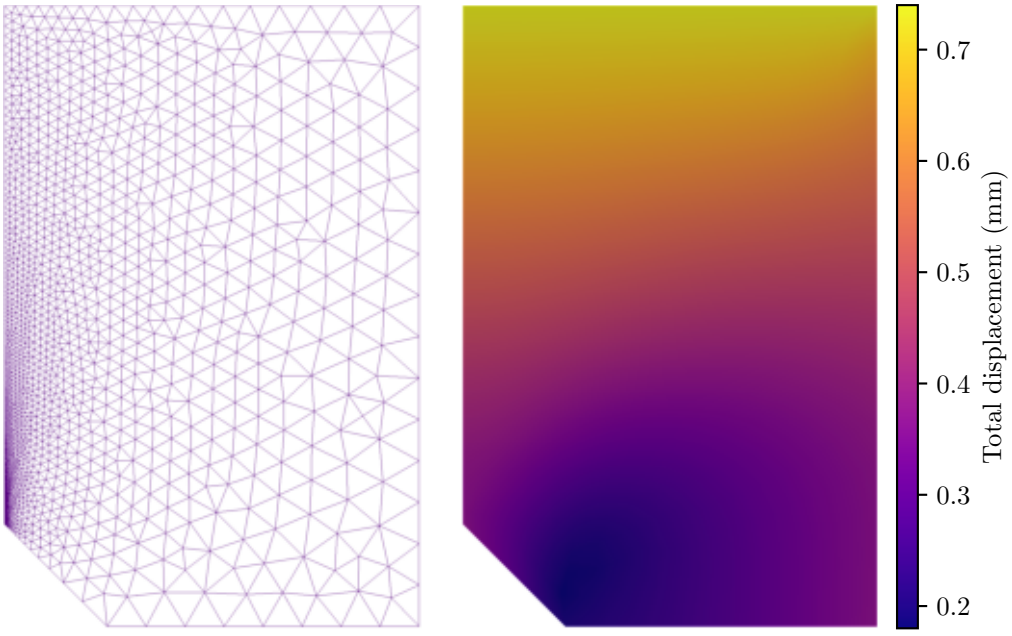

Figure 12: The mesh of the rhombus hole specimen, and the total displacements of the mesh at the end of the test.

The loading protocol is to impose a vertical displacement of a rate of 1 mm/s on the top edge, while also enforcing a no-slip condition, so that the horizontal velocities on the top edge are zero. At the time the first node cracks (i.e. $\beta \leqslant 1 \times 10^{-12}$), the vertical loading is stopped and the displacement is held constant. The simulation continues until 20 time-steps have passed with no changes in the value of β in any of the cohesive zone nodes.

The simulation is carried out with the values in Doitrand et al. (2019) representing PMMA, namely a Young's modulus $E = 1600$ MPa, a Poisson's ratio $\nu = 0.37$, a density $\rho = 1.19 \times 10^{-3}$ g/mm^3, a critical traction $\sigma_c = 80$ MPa, a fracture energy $G_c = 0.25$ N/mm, and a coefficient of restitution $e = 0$.

We can plot the results of the simulation in terms of the crack progression, once more tracking results at the points of interest, which in this case are the point at which the crack begins (index 0), the point at which the crack arrests (index 4), and the quarter, half and three-quarter points between them (indices 1, 2, and 3, respectively).

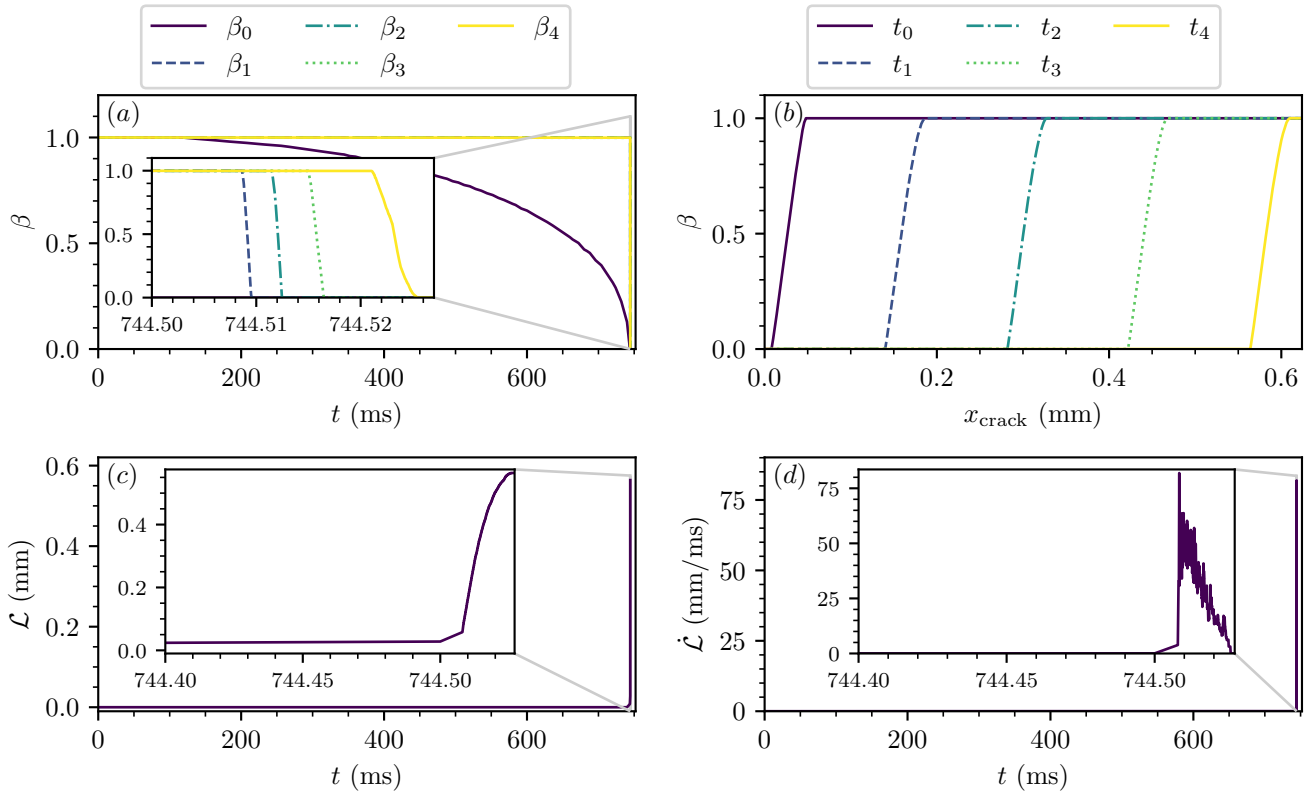

Figure 13: The simulation of a rhombus hole specimen. (a) The cohesion β as a function of time t at the quarter points. (b) The cohesion β as a function of distance from the tip of the initial crack x_{crack}, at the time that each of the quarter points goes to zero. (c) The length L of the crack as a function of time t. (d) The crack tip velocity $\dot{L}$ as a function of time t.

In this case, we observe several interesting behaviours in Figure 13. Unlike the relatively steady decohesion observed in the DCB, we observe that the node at the corner of the rhombus hole steadily decoheres over a long period of time, but once it reaches zero and the crack begins growing, the speed of decohesion is rapid (shown in the inset to (a)). Similarly, when considering the spatial distribution of the cohesion variable at the time each quarter point is fully decohered, we see that the length of the fracture process zone is essentially constant, as is the case with the DCB. Unlike the DCB, there is a small period where the crack growth is relatively small, before a period of rapid growth. The final phase is a steady decrease in crack growth rate, followed by the crack arrest. The final crack arrest length is 0.564 mm, which compares well with the value of 0.593 obtained by Doitrand et al. (2019).

Once again, we may also study the energetic properties of the solution algorithm that we implement:

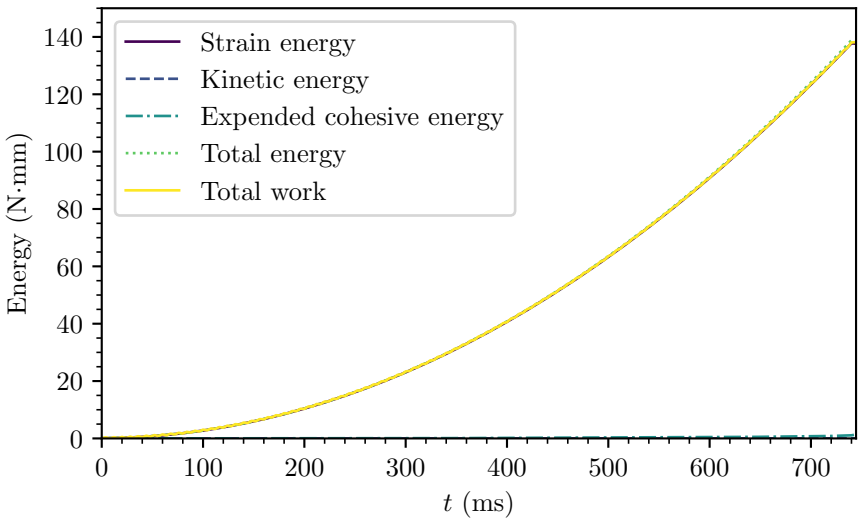

Figure 14: The energies of the rhombus hole simulation.

We can see that the majority of work accounts for strain energy, and the total energy is simply the sum of the strain and kinetic energies. The kinetic energy is negligible, while the expended cohesive energy remains very small relative to the overall work input.

As a final point of comparison, we may follow Doitrand et al. (2019), and vary the rhombus hole angle γ while observing the effect on the crack initiation force F_{init} and the crack arrest length $\mathcal{L}_{\text{arrest}}$.

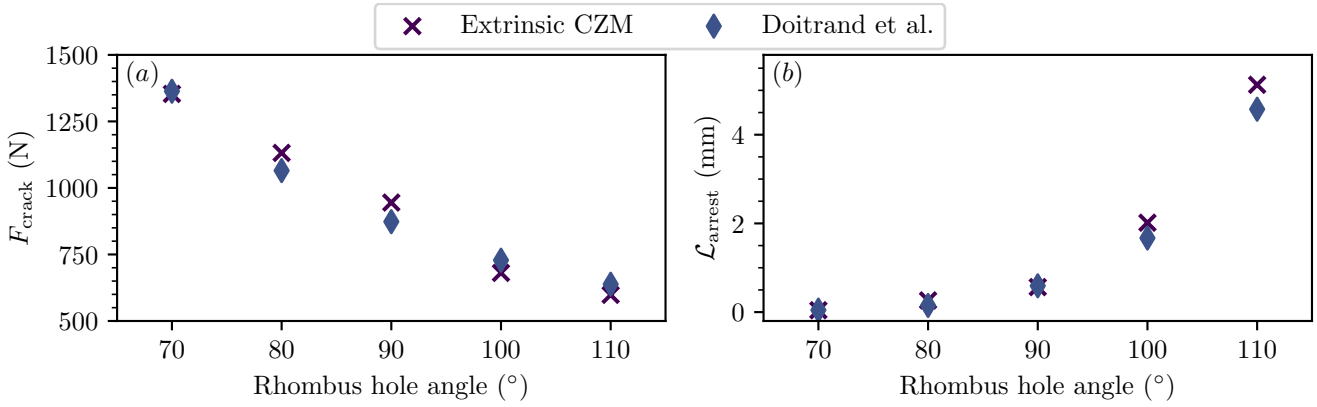

Figure 15: The results of simulations varying the rhombus hole angle γ. (a) The crack initiation force F_{init} at which cracking begins. (b) The crack arrest length $\mathcal{L}$ at which crack propagation stops, in the absence of continued loading.

We may observe in Figure 15 that there is a very good agreement between the results of the simulations in Doitrand et al. (2019), and the results of our models, with the initiation force decreasing and crack arrest length increasing as the rhombus hole angle increases. Possible reasons that may account for the minor differences may be the effects of dimensionality, the initial rigidity present in the cohesive zone model used by Doitrand et al. (2019) (they allocated an initial stiffness of 1×10^8 MPa/mm), and different meshes used to simulate the results.

6 Conclusions

In this paper, we first used the principle of virtual power to establish the equilibrium and boundary conditions of a body with a cohesive zone. Then, we postulated a free energy potential for the surface that allowed us to obtain non-smooth state laws of the system. These state laws describe extrinsic cohesive zone models that do not have the "shifted intrinsic model" structure, thus guaranteeing appropriate physical behaviour under complex dynamic loading. By appropriately specifying a dissipative pseudo-potential, we obtained a complete generalised constitutive model of the cohesive zone system, and demonstrated that while decohesion is an irreversible process, it is also non-dissipative. We then specified a particular energetic potential in order to obtain a linear evolution of the cohesion variable with the displacement jump across the crack.

By appropriately discretising our system, and working with differential measures, we were able to include non-smooth impact dynamics within our model. The discretised system was combined with a θ-method to obtain a time-stepping scheme that could be formulated as a linear complementarity problem. We then proved that the problem was well posed for a sufficiently small time step, meaning that a solution exists, and that it is unique for certain variables.

We then implemented the model numerically by solving the complementarity problem at each time step. We demonstrated the system in statics, firstly parameter values leading to a well-posed problem, and then with values leading to an ill-posed problem. We then demonstrated that the same system in dynamics remains well-posed. Finally, we simulated some physical systems of interest by combining the linear complementarity problem with the finite element method. Both a double cantilever beam, and a rhombus-hole sample were satisfactorily resolved, with the numerical scheme demonstrating good integration properties. The results of the rhombus hole simulations compared well with those of other authors in the literature.

This work has demonstrated that applications of convex analysis can lead to physically correct and numerically efficient models for crack propagation. Natural extensions of this work are to generalise the model to tangential displacements, adopt other possible forms of the cohesion evolution law, and to combine crack propagation with other physical phenomena.

Acknowledgements The authors thank Aurelian Doitrand, Rafael Estevez and Dominique Leguillon for kindly providing their data.
This work was carried out as part of Project SMART-PROTECT, financed by the Auvergne-Rhône-Alpes region.

A Boundary conditions in the stiffness matrix

If we have our system

$$Kq = F + H^\top r_{\text{N}}, \tag{77}$$

typically K is singular and we can't invert. We want to create a modified system that takes account of the boundary conditions and inserts them into the stiffness matrix to create a modified system

$$\bar{K}q = \bar{F} + H^\top r_{\text{N}} \tag{78}$$

Supposing we know a given displacement q_i is enforced to be $\bar{q}_i$, which could be due to a Dirichlet boundary condition or a controlled displacement, we want to create the matrix $\bar{K}$ so that

$$\bar{K} = \begin{bmatrix} K_{11} & \dots & 0 & \dots & K_{1n} \\ \vdots & \ddots & \vdots & \ddots & \vdots \\ 0 & \dots & K_{ii} & \dots & 0 \\ \vdots & \ddots & \vdots & \ddots & \vdots \\ K_{n1} & \dots & 0 & \dots & K_{nn} \end{bmatrix}, \tag{79}$$

i.e. $\bar{K} = K$ except for the row and column corresponding to enforced displacement $\bar{q}_i$, where all entries are set to zero other than K_{ii}.

To compensate for this change in the stiffness matrix, the removed terms are shifted across to a modified force vector $\bar{F}$ such that

$$\bar{F} = \begin{bmatrix} F_1 - K_{1i}\bar{q}_i \\ \vdots \\ K_{ii}\bar{q}_i \\ \vdots \\ F_n - K_{ni}\bar{q}_i \end{bmatrix}, \tag{80}$$

thus leaving the system in equilibrium. The full displacement vector can then be obtained by

$$q = \bar{K}^{-1}\left(\bar{F} + H^\top r_{\text{N}}\right), \tag{81}$$

as $\bar{K}$ is in general non-singular and thus invertible.

To enforce the boundary conditions in dynamics a corresponding operation is carried out on the augmented mass matrix $\hat{M} = M + h^2\theta^2 K$ to create

$$\bar{\hat{M}} = \begin{bmatrix} \hat{M}_{11} & \dots & 0 & \dots & \hat{M}_{1n} \\ \vdots & \ddots & \vdots & \ddots & \vdots \\ 0 & \dots & \hat{M}_{ii} & \dots & 0 \\ \vdots & \ddots & \vdots & \ddots & \vdots \\ \hat{M}_{n1} & \dots & 0 & \dots & \hat{M}_{nn} \end{bmatrix}. \tag{82}$$

The enforced velocities $\bar{v}_k$ are included in the modified free-flight impulse $\bar{\hat{i}}$ by

$$\bar{\hat{i}} = \begin{bmatrix} \hat{i}_1 - \hat{M}_{1k}\bar{v}_k \\ \vdots \\ \hat{M}_{kk}\bar{v}_k \\ \vdots \\ \hat{i}_n - \hat{M}_{nk}\bar{v}_k \end{bmatrix}, \tag{83}$$

which produces nodal impulses that cause the enforced velocities to be respected.

References

Acary, V. and Y. Monerie (2006). *Nonsmooth fracture dynamics using a cohesive zone approach*. Anglais. Research Report RR-6032. INRIA, p. 56. URL: http://hal.inria.fr/inria-00110560/en/.

Ashouri Vajari, Danial, Brian Nyvang Legarth, and Christian F. Niordson (Nov. 2013). "Micromechanical modeling of unidirectional composites with uneven interfacial strengths". In: *European Journal of Mechanics, A/Solids* 42, pp. 241–250. ISSN: 09977538. DOI: 10.1016/j.euromechsol.2013.06.008.

Azab, Marc, Guillaume Parry, and Rafael Estevez (Mar. 2020). "An analytical model for DCB/wedge tests based on Timoshenko beam kinematics for accurate determination of cohesive zone lengths". In: *International Journal of Fracture* 222.1-2, pp. 137–153. ISSN: 15732673. DOI: 10.1007/s10704-020-00438-2. URL: https://doi.org/10.1007/s10704-020-00438-2.

Berman, Neri, Gil Cohen, and Jay Fineberg (2020). "Dynamics and properties of the cohesive zone in rapid fracture and friction". In: *Physical Review Letters* 125.12, p. 125503. ISSN: 10797114. DOI: 10.1103/PhysRevLett.125.125503. URL: https://doi.org/10.1103/PhysRevLett.125.125503.

Bybordiani, Milad and Daniel Dias-da-Costa (Apr. 2021). "A consistent finite element approach for dynamic crack propagation with explicit time integration". In: *Computer Methods in Applied Mechanics and Engineering* 376, p. 113652. ISSN: 00457825. DOI: 10.1016/j.cma.2020.113652. URL: https://doi.org/10.1016/j.cma.2020.113652%20https://linkinghub.elsevier.com/retrieve/pii/S0045782520308379.

Camacho, G.T. and M. Ortiz (1996). "Computational modelling of impact damage in brittle materials". In: *International Journal of Solids and Structures* 33.20, pp. 2899–2938. ISSN: 0020-7683. DOI: https://doi.org/10.1016/0020-7683(95)00255-3. URL: http://www.sciencedirect.com/science/article/pii/0020768395002553.

Carter, Bruce et al. (2000). "Parallel FEM simulation of crack propagation-challenges, status, and perspectives". In: *Lecture Notes in Computer Science (including subseries Lecture Notes in Artificial Intelligence and Lecture Notes in Bioinformatics)*. Vol. 1800 LNCS. Springer Verlag, pp. 443–449. ISBN: 354067442X. DOI: 10.1007/3-540-45591-4_59.

Célarié, F. et al. (2003). "Glass Breaks like Metal, but at the Nanometer Scale". In: *Physical Review Letters* 90.7, p. 4. ISSN: 10797114. DOI: 10.1103/PhysRevLett.90.075504.

Chaboche, J. L., F. Feyel, and Y. Monerie (2001). "Interface debonding models: A viscous regularization with a limited rate dependency". In: *International Journal of Solids and Structures* 38.18, pp. 3127–3160. ISSN: 00207683. DOI: 10.1016/S0020-7683(00)00053-6.

Cottle, Richard W., Jong-Shi Pang, and Richard E. Stone (2009). *The Linear Complementarity Problem*. Ed. by Robert E. O'Malley. Second. Philadelphia: Society for Industrial and Applied Mathematics, p. 781. ISBN: 978-0-89871-686-3. DOI: 10.1137/1.9780898719000. URL: http://epubs.siam.org/doi/book/10.1137/1.9780898719000.

Doitrand, Aurélien, Rafael Estevez, and Dominique Leguillon (Feb. 2019). "Comparison between cohesive zone and coupled criterion modeling of crack initiation in rhombus hole specimens under quasi-static compression". In: *Theoretical and Applied Fracture Mechanics* 99.November 2018, pp. 51–59. ISSN: 01678442. DOI: 10.1016/j.tafmec.2018.11.007. URL: https://doi.org/10.1016/j.tafmec.2018.11.007%20https://linkinghub.elsevier.com/retrieve/pii/S0167844218304725.

Doitrand, Aurélien et al. (Jan. 2021). "Experimental and theoretical characterization of mixed mode brittle failure from square holes". In: *International Journal of Fracture*, pp. 1–11. ISSN: 15732673. DOI: 10.1007/s10704-020-00512-9. URL: https://doi.org/10.1007/s10704-020-00512-9.

Espinha, Rodrigo et al. (2013). "Scalable parallel dynamic fracture simulation using an extrinsic cohesive zone model". In: *Computer Methods in Applied Mechanics and Engineering* 266, pp. 144–161. ISSN: 0045-7825. DOI: https://doi.org/10.1016/j.cma.2013.07.008. URL: http://www.sciencedirect.com/science/article/pii/S0045782513001783.

Falk, M.L., A. Needleman, and J.R. Rice (2001). "A critical evaluation of dynamic fracture simulations using cohesive surfaces". In: *Jounal de Physique IV, (in press) 2001*.

Frémond, Michel (1988). "Contact with Adhesion". In: *Nonsmooth Mechanics and Applications*. Vienna: Springer Vienna, pp. 177–221. DOI: 10.1007/978-3-7091-2624-0_3. URL: http://link.springer.com/10.1007/978-3-7091-2624-0_3.

— (2002). *Non-Smooth Thermomechanics*. Berlin, Heidelberg: Springer Berlin Heidelberg. ISBN: 978-3-642-08578-9. DOI: 10.1007/978-3-662-04800-9. URL: http://link.springer.com/10.1007/978-3-662-04800-9.

— (2012a). "Contact with Adhesion". In: *Phase Change in Mechanics*. Vol. 13. Lecture Notes of the Unione Matematica Italiana 4. Berlin, Heidelberg: Springer Berlin Heidelberg, pp. 151–156. ISBN: 978-3-642-24608-1. DOI: 10.1007/978-3-642-24609-8. URL: http://link.springer.com/10.1007/978-3-642-24609-8.

— (2012b). "Damage of Solids Glued on One Another: Coupling of Volume and Surface Damages". In: *Phase Change in Mechanics*. Lecture Notes of the Unione Matematica Italiana. Berlin, Heidelberg: Springer Berlin Heidelberg, pp. 115–130. ISBN: 978-3-642-24608-1. DOI: 10.1007/978-3-642-24609-8. URL: http://link.springer.com/10.1007/978-3-642-24609-8.

Griffith, Alan Arnold (Jan. 1921). "The phenomena of rupture and flow in solids". In: *Philosophical Transactions of the Royal Society of London. Series A: Mathematical, Physical and Engineering Sciences* 221.582-593, pp. 163–198. ISSN: 0264-3952. DOI: 10.1098/rsta.1921.0006. URL: https://royalsocietypublishing.org/doi/10.1098/rsta.1921.0006.

Guilloteau, E, H Charrue, and F Creuzet (1996). "The direct observation of the core region of a propagating fracture crack in glass". In: *Europhysics Letters (EPL)* 34.7, pp. 549–554. ISSN: 0295-5075. DOI: 10.1209/epl/i1996-00493-3.

Houlsby, Guy T. (2019). "Frictional Plasticity in a Convex Analytical Setting". In: *Open Geomechanics* 1.3, pp. 1–10. DOI: 10.5802/ogeo.2. URL: https://opengeomechanics.centre-mersenne.org/item/OGEO_2019__1__A3_0.

Jean, Michel and Jean Jacques Moreau (1992). "Unilaterality and dry friction in the dynamics of rigid body collections". In: *1st Contact Mechanics International Symposium*. Ed. by A. Curnier. Lausanne, pp. 31–48. URL: https://hal.archives-ouvertes.fr/hal-01863710.

Kubair, D.V. and P.H. Geubelle (2003). "Comparative analysis of extrinsic and intrinsic cohesive models of dynamic fracture". In: *International Journal of Solids and Structures* 40.15, pp. 3853–3868. ISSN: 0020-7683. DOI: https://doi.org/10.1016/S0020-7683(03)00171-9. URL: http://www.sciencedirect.com/science/article/pii/S0020768303001719.

Marigo, Jean-Jacques (1981). "Formulation d'une loi d'endommagement d'un materiau élastique". In: *Comptes rendus de l'Académie des sciences. Série 2, Mécanique, Physique, Chimie, Sciences de l'univers, Sciences de la Terre* 292.May, pp. 1309–1312.

Michel, J C and P Suquet (May 1994). "An analytical and numerical study of the overall behaviour of metal-matrix composites". In: *Modelling and Simulation in Materials Science and Engineering* 2.3A, p. 637. ISSN: 0965-0393. DOI: 10.1088/0965-0393/2/3A/015. URL: https://iopscience.iop.org/article/10.1088/0965-0393/2/3A/015%20https://iopscience.iop.org/article/10.1088/0965-0393/2/3A/015/meta.

Moreau, J. J. (July 1999). "Numerical aspects of the sweeping process". In: *Computer Methods in Applied Mechanics and Engineering* 177.3-4, pp. 329–349. ISSN: 0045-7825. DOI: 10.1016/S0045-7825(98)00387-9.

Moreau, Jean Jacques (1970). "Sur les lois de frottement, de plasticité et de viscosité". In: *Comptes rendus de l'Académie des sciences. Série A - Sciences mathématiques* 271, pp. 608–611.

— (1974). "On Unilateral Constraints, Friction and Plasticity". In: *New Variational Techniques in Mathematical Physics*. Springer Berlin Heidelberg, pp. 171–322. DOI: 10.1007/978-3-642-10960-7_7. URL: https://link.springer.com/chapter/10.1007/978-3-642-10960-7_7.

— (1986). "Une formulation du contact à frottement sec; application au calcul numérique". In: *Comptes rendus de l'Académie des sciences. Série 2, Mécanique, Physique, Chimie, Sciences de l'univers, Sciences de la Terre* 302.13, pp. 799–801. ISSN: 0764-4450.

Murphy, N. and A. Ivankovic (2005). "The prediction of dynamic fracture evolution in PMMA using a cohesive zone model". In: *Engineering Fracture Mechanics* 72.6. Prospects in Fracture Papers from a Conference held to Celebrate the 65th Birthday of Professor J.G. Williams, FRS, FREng Imperial College London, July 2003, pp. 861–875. ISSN: 0013-7944. DOI: https://doi.org/10.1016/j.engfracmech.2004.08.001. URL: http://www.sciencedirect.com/science/article/pii/S001379440400195X.

Nguyen, Vinh Phu (2014). "Discontinuous Galerkin/extrinsic cohesive zone modeling: Implementation caveats and applications in computational fracture mechanics". In: *Engineering Fracture Mechanics* 128, pp. 37–68. ISSN: 0013-7944. DOI: https://doi.org/10.1016/j.engfracmech.2014.07.003. URL: http://www.sciencedirect.com/science/article/pii/S0013794414002136.

Nguyen, Vinh Phu and Jian Ying Wu (Oct. 2018). "Modeling dynamic fracture of solids with a phase-field regularized cohesive zone model". In: *Computer Methods in Applied Mechanics and Engineering* 340, pp. 1000–1022. ISSN: 00457825. DOI: 10.1016/j.cma.2018.06.015.

Okubo, Kurama et al. (Nov. 2019). "Dynamics, Radiation, and Overall Energy Budget of Earthquake Rupture With Coseismic Off-Fault Damage". In: *Journal of Geophysical Research: Solid Earth* 124.11, pp. 11771–11801. ISSN: 2169-9313. DOI: 10.1029/2019JB017304. arXiv: 1901.01771. URL: https://onlinelibrary.wiley.com/doi/10.1029/2019JB017304.

Papoulia, Katerina D., Chin-Hang Sam, and Stephen A. Vavasis (Oct. 2003). "Time continuity in cohesive finite element modeling". In: *International Journal for Numerical Methods in Engineering* 58.5, pp. 679–701. ISSN: 0029-5981. DOI: 10.1002/nme.778. URL: http://doi.wiley.com/10.1002/nme.778.

Parrinello, Francesco (Sept. 2020). "Hybrid equilibrium element with interelement interface for the analysis of delamination and crack propagation problems". In: *International Journal for Numerical Methods in Engineering* August. ISSN: 0029-5981. DOI: 10.1002/nme.6531. URL: https://onlinelibrary.wiley.com/doi/10.1002/nme.6531.

Parrinello, Francesco and Guido Borino (2020). "Cohesive-frictional interface in an equilibrium based finite element formulation". In: *Proceedings of XXIV AIMETA Conference 2019*. Ed. by Antonio Carcaterra, Achille Paolone, and Giorgio Graziani. Lecture Notes in Mechanical Engineering September. Cham: Springer International Publishing, pp. 419–426. ISBN: 978-3-030-41056-8. DOI: 10.1007/978-3-030-41057-5. URL: http://link.springer.com/10.1007/978-3-030-41057-5.

Sam, Chin-Hang, Katerina D. Papoulia, and Stephen A. Vavasis (Sept. 2005). "Obtaining initially rigid cohesive finite element models that are temporally convergent". In: *Engineering Fracture Mechanics* 72.14, pp. 2247–2267. ISSN: 00137944. DOI: 10.1016/j.engfracmech.2004.12.008. URL: https://linkinghub.elsevier.com/retrieve/pii/S0013794405000808.

Seagraves, A. and R. Radovitzky (2010). *Advances in cohesive zone modeling of dynamic fracture*, pp. 349–405. DOI: 10.1007/978-1-4419-0446-1_12.

Versino, Daniele et al. (2015). "A thermodynamically consistent discontinuous Galerkin formulation for interface separation". In: *Composite Structures* 133, pp. 595–606. ISSN: 0263-8223. DOI: https://doi.org/10.1016/j.compstruct.2015.07.080. URL: http://www.sciencedirect.com/science/article/pii/S0263822315006261.

Xu, X.-P. and A. Needleman (Sept. 1994). "Numerical simulations of fast crack growth in brittle solids". In: *Journal of the Mechanics and Physics of Solids* 42.9, pp. 1397–1434. ISSN: 00225096. DOI: 10.1016/0022-5096(94)90003-5. URL: https://linkinghub.elsevier.com/retrieve/pii/0022509694900035.

Zhang, Zhengyu (Jenny), Glaucio H. Paulino, and Waldemar Celes (Nov. 2007). "Extrinsic cohesive modelling of dynamic fracture and microbranching instability in brittle materials". In: *International Journal for Numerical Methods in Engineering* 72.8, pp. 893–923. ISSN: 00295981. DOI: 10.1002/nme.2030. URL: http://doi.wiley.com/10.1002/nme.2030.

Zhou, F. and J. F. Molinari (Jan. 2004a). "Dynamic crack propagation with cohesive elements: a methodology to address mesh dependency". In: *International Journal for Numerical Methods in Engineering* 59.1, pp. 1–24. ISSN: 0029-5981. DOI: 10.1002/nme.857. URL: http://doi.wiley.com/10.1002/nme.857.

Zhou, Fenghua and Jean Francois Molinari (Nov. 2004b). "Stochastic fracture of ceramics under dynamic tensile loading". In: *International Journal of Solids and Structures* 41.22-23, pp. 6573–6596. ISSN: 00207683. DOI: 10.1016/j.ijsolstr.2004.05.029.